

Polarised neutron diffraction measurements of $\text{PrBa}_2\text{Cu}_3\text{O}_{6+x}$ and the Bayesian statistical analysis of such data

Anders Johannes Markvardsen
St. Edmund Hall

A thesis submitted for the degree of
Doctor of Philosophy at the
University of Oxford



Clarendon Laboratory
September 2000

Chapter 5

Polarised neutron diffraction data from $\text{PrBa}_2\text{Cu}_3\text{O}_{6+x}$

This chapter describes the analysis of a polarised neutron diffraction data set measured on a single crystal of $\text{PrBa}_2\text{Cu}_3\text{O}_{6.24}$. These data were discussed in the short paper [82]. Here, a more detailed discussion is presented using an improved data analysis technique for inverting the measured magnetic structure factors into magnetization density image, and additional theoretical calculations have been performed to help in the interpretation of the magnetization density images. The original purpose for investigating the magnetization density in $\text{PrBa}_2\text{Cu}_3\text{O}_{6+x}$ was to look for evidence of a hybridisation of the Pr $4f$ electrons with electronic states in the CuO_2 planes, as has been predicted by a number of theoretical works to cause the suppression of superconductivity in $\text{PrBa}_2\text{Cu}_3\text{O}_{6+x}$. However, very little evidence is found which can support such an hybridisation. Of interest also, is that a number of other moments, with significant magnitude, are observed in the unit cell, which cannot be accounted for by existing theoretical work describing the suppression of superconductivity in $\text{PrBa}_2\text{Cu}_3\text{O}_{6+x}$. Such observed features may prove useful in helping theoreticians to suggest new theoretical models for $\text{PrBa}_2\text{Cu}_3\text{O}_{6+x}$.

5.1 Introduction to the $\text{PrBa}_2\text{Cu}_3\text{O}_{6+x}$ problem

It has been known for more than 10 years that the substitution of Pr for Y in $\text{YBa}_2\text{Cu}_3\text{O}_{6+x}$ causes a suppression of superconductivity in that compound [1]. Despite intensive research it is still not known what causes this effect, the main reason why it remains of strong interest is because of its relevance to the physics of high- T_c superconductivity. For a very recent review on $\text{PrBa}_2\text{Cu}_3\text{O}_{6+x}$ see Ref. [1]. Many aspects of $\text{PrBa}_2\text{Cu}_3\text{O}_{6+x}$ have been studied experimentally and many theoretical models have been proposed (see also the older review paper in Ref. [93]). For instance, the magnetic ordering of the Pr and Cu moments are now well understood experimentally, but still not theoretically [1]. The aspect of $\text{PrBa}_2\text{Cu}_3\text{O}_{6+x}$ which will be studied is its magnetic field induced magnetization density. The original purpose of this study was to make a comparison between the observed induced magnetization density and theoretical models which predict electric interactions between Pr and the superconducting CuO_2 planes.

A common theoretical model used for explaining suppression of superconductivity by Pr in $\text{Pr}_y\text{Y}_{1-y}\text{Ba}_2\text{Cu}_3\text{O}_{6+x}$ involves the valence state of the Pr ions. Pr is situated at the centre of the unit cell in Fig. 5.1 and for superconducting isostructural compounds of $\text{PrBa}_2\text{Cu}_3\text{O}_{6+x}$ this site is normally occupied by ions with a 3+ oxidation state (like Y^{3+} or most other rare earths), but if Pr were more highly ionised then holes in the CuO_2 planes could be neutralised and the number of mobile charge carriers reduced below the level needed to sustain superconductivity. In this context the most influential work has been that of Fehrenbacher & Rice [94] who proposed a hybrid state containing stable Pr^{3+} and an intermediate valence $\text{Pr}(\text{IV})$ state made from a linear combination of Pr^{4+} and $\text{Pr}^{3+}\underline{L}$, where \underline{L} denotes a ligand hole in the neighbouring oxygen $2p$ orbitals. Such a model involves changes in the electronic structure of the Pr ions as compared to that of Pr ions without interaction with the CuO_2 layers. Information on the spatial distribution of the 4f electrons of Pr would therefore be valuable to test models of

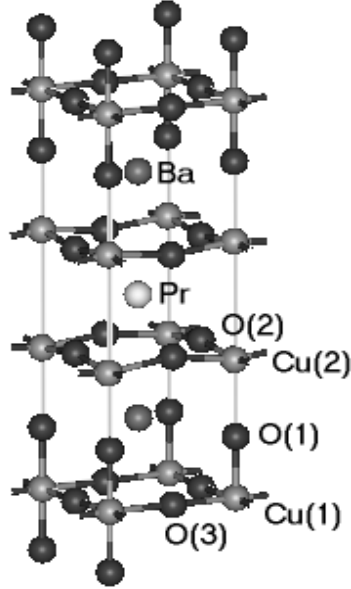


Figure 5.1: Shows the unit cell of $\text{PrBa}_2\text{Cu}_3\text{O}_{6+x}$ in its tetragonal phase. For the temperature parameters in table 5.1 it is assumed that the y -axis points in the O(3)-Cu(1) direction and the x -axis in the Cu(2)-O(2) direction.

this kind, this information can be obtained by polarised neutron diffraction. That was our original motivation for performing the PND measurements presented in this chapter.

5.2 Data collection for $\text{PrBa}_2\text{Cu}_3\text{O}_{6.24}$

A crystal of $\text{PrBa}_2\text{Cu}_3\text{O}_{6.24}$ with mass 23 mg was selected from the same batch as used in recent studies of the magnetic ordering[95]. To obtain a set of magnetic structure factors, unpolarised neutron diffraction and polarised neutron diffraction measurements were performed using the D9 and D3 instruments at Institut Laue-Langevin (ILL), Grenoble. The unpolarised measurements were done to refine the crystal structure and extinction parameters. The data was collected on a four-circle multidetector diffractometer, the detector being a gas-filled two-dimensional multiwire proportional counter. The crystal was mounted in an Air

Product two-stage Displex cryorefrigerator and the sample was cooled down to $T = 20K$. 989, 1234 and 697 reflections were scanned at wavelengths 0.8389\AA , 0.70\AA and 0.54\AA respectively. Different wavelengths were used in order to estimate the amount of extinction. The three-dimensional arrays of counts observed around each scanned reflection were corrected for background and reduced to squared structure amplitudes using the three-dimensional integration method of Wilkinson et al. [96]. Contamination from neighbouring reflections, a potential problem at the shorter wavelengths, was avoided by limiting the integration of each reflection to extend no further than half way to the neighbouring reflections. Averaging over repeated measurements and equivalent reflections gave 410, 648 and 412 reflections at the three wavelengths. After correcting for extinction and absorption a least squares refinement program (UPALS) was used to refine the nuclear structure against the data at all three wavelengths simultaneously¹. The position, anisotropic temperature parameters and fractional occupancy of each site in the unit cell are listed in table 5.1.

The polarised neutron diffraction was also carried out at $T = 20K$, this is well above the antiferromagnetic ordering temperature of the Pr sublattice ($T_N = 12K$ [95]). The setup of the polarised experiment is discussed in Chap. 1. The wavelength of the neutrons was 0.843\AA and an applied magnetic field \mathbf{B} of 4.6 T was used over the sample. In order to access a large amount of reciprocal space, the experiment was carried out using two orientations of the crystal relative to the applied field: \mathbf{B} parallel to $[1\ 0\ 0]$, i.e. $\mathbf{B} \parallel [1\ 0\ 0]$, and \mathbf{B} parallel to $[1\ 1\ 0]$, i.e. $\mathbf{B} \parallel [1\ 1\ 0]$. Because the crystal structure is tetragonal, the magnitude of the induced moment is expected to be parallel to the applied field and the same for both orientations on a macroscopic scale. With $\mathbf{B} \parallel [1\ 0\ 0]$ and $\mathbf{B} \parallel [1\ 1\ 0]$, 61 and 56 unique flipping ratios were measured respectively. To convert these flipping ratios into magnetic structure factors the CCSL program SORGAM was used.

¹Many thanks to Garry McIntyre for doing this.

atom	position (z-component)	temperature parameters	site occupancy
Pr	0.5	$B_{11} = 0.0864(159)$ $B_{33} = 0.1704(234)$	1
Ba	0.19171(6)	$B_{11} = 0.3386(113)$ $B_{22} = 0.4955(184)$	1
Cu(1)	0	$B_{11} = 0.6158(128)$ $B_{33} = 0.2695(161)$	1
Cu(2)	0.35224(4)	$B_{11} = 0.1394(67)$ $B_{33} = 0.3374(106)$	1
O(1)	0.15288(7)	$B_{11} = 1.5016(170)$ $B_{33} = 0.4888(167)$	1
O(2)	0.36970(4)	$B_{11} = 0.2236(99)$ $B_{22} = 0.3462(106)$ $B_{33} = 0.4983(100)$	1
O(3)	0	$B_{11} = 0.876(190)$ $B_{22} = 0.663(173)$ $B_{33} = 0.548(156)$	0.1222(55)

Table 5.1: Refined fractional atomic coordinates, thermal parameters and site occupancies are listed. The anisotropic temperature factor has the form $\exp(-h^2 B_{11}/4a^2 - k^2 B_{22}/4b^2 - l^2 B_{33}/4c^2)$, where the units of the B_{ii} are \AA^2 . The space group of $\text{PrBa}_2\text{Cu}_3\text{O}_{6.24}$ is $P4/\text{mmm}$ and the lattice parameters refined to $a = 3.8982(3)\text{\AA}$ and $c = 11.7976(10)\text{\AA}$. Residuals for the refinement were $R_w(F^2) = 7.7\%$, $R(F) = 3.6\%$ and goodness of fit = 2.52, see e.g. Ref [97],[98] for the formal definition of these quantities. The site occupations of Pr, Cu(1), Cu(2) and O(1) were also varied, but the values stayed within two esd's of the stoichiometric values. Notice that the displacement parameters of O(1) are surprisingly large. The parameters for O(3) are also large, but the site is only slightly occupied. The extinction parameter was 265.8 sec RMS mosaic.

SORGAM takes flipping ratios as input and structural information about the position of nuclei, extinction² and absorption parameters etc.. Structural information for PrBa₂Cu₃O_{6.24} is listed in table 5.1. The resulting magnetic structure factors are listed in table 5.5 except for the 13 structure factors which have the same Miller indices for both **B** field orientations, these are listed separately in table 5.6. In table 5.6 an estimated ‘average’ value of each of these 13 Miller indices is listed in the last column, taken to be the arithmetic mean: $\bar{F}_{hkl} = (F_{hkl}^{B \parallel [1\ 0\ 0]} + F_{hkl}^{B \parallel [1\ 1\ 0]})/2$ and $\bar{\sigma}_{hkl} = (\sigma_{hkl}^{B \parallel [1\ 0\ 0]} + \sigma_{hkl}^{B \parallel [1\ 1\ 0]})/2$. For the two reflections with Miller indices (0, 0, 11) and (−1, 3, 0), $\bar{\sigma}_{hkl}$ is further increased to the value $\bar{\sigma}_{hkl} = |\bar{F}_{hkl} - F_{hkl}^{B \parallel [1\ 0\ 0]}|$. These 13 ‘averaged’ structure factor values and standard deviations are estimated with the aim of accounting for possible differences in the induced moment distributions in the unit cell when applying **B** \parallel [1 0 0] and **B** \parallel [1 1 0]. In addition to the magnetic structure factors obtained from polarised neutron diffraction the zero-*q* structure factor (with Miller indices (0, 0, 0)), which is equal to the total moment in the unit cell, was determined from a bulk magnetisation (SQUID) measurement on the same crystal of PrBa₂Cu₃O_{6.24} also at $T = 20K$ and $B = 4.6T$ ³. The zero-*q* structure factor was measured to be $0.283 \pm 0.011\mu_B$. The complete set of unique magnetic structure factors for PrBa₂Cu₃O_{6.24} will be analysed both as a whole and as two independent data sets.

5.3 Crystal field calculation and comparison with two data sets

The two independently measured PND data set for PrBa₂Cu₃O_{6.24} with **B** \parallel [1 0 0] and **B** \parallel [1 1 0] are analysed separately in this section using the Bayesian image

²Many thanks to Bruce Forsyth (one of the authors of the CCSL suite) who helped with the insertion of the extinction parameter from the UPALS refinement into SORGAM.

³Many thanks to Steven Lister for doing this.

analysis method of Chap. 4, and the resulting magnetization density maps are compared. To help assess whether the density maps show evidence of an interaction between the Pr $4f$ electrons and electronic states in the CuO_2 planes a theoretical calculation is performed. The basis for the theoretical calculation is discussed in the next subsection, in subsection 5.3.2 the theoretical and experimental densities are compared.

5.3.1 Crystal field model for Pr^{3+}

The induced magnetization density in $\text{PrBa}_2\text{Cu}_3\text{O}_{6.24}$ will mainly originate from Pr. Pr is believed to be in a Pr^{3+} valence state (or in a mixture of $\text{Pr}^{3+}/\text{Pr}^{4+}$ with the majority of Pr being in the $3+$ valence state), Pr^{3+} is a magnetic ion with an open $4f$ electron shell containing two electrons. These two electrons may hybridise with electronic states of the CuO_2 planes and cause suppression of superconductivity as, for example, is claimed by the theoretical work in Ref. [94]. If this is true, such a hybridisation will result in a distortion of the Pr^{3+} $4f$ electron density from that expected for an isolated Pr^{3+} ion under the influence of the local crystal field. To assist such an investigation, the magnetization density of an isolated Pr^{3+} ion in the local crystal field of $\text{PrBa}_2\text{Cu}_3\text{O}_{6.24}$ is calculated.

The magnetization density of Pr^{3+} is calculated by evaluating the quantum expectation value of magnetization density operators with respect to a specified wave function. Thus, the first step is to determine the wave function for Pr^{3+} in $\text{PrBa}_2\text{Cu}_3\text{O}_{6.24}$ at $T = 20\text{K}$, with an applied field of $B = 4.6\text{T}$, from a model taking into account the local crystal field. Pr is a rare earth and is well described within the intermediate coupling angular momentum scheme because the mean radius of the $4f$ electrons is small and the dominating interaction is the Coulomb repulsion between the $4f$ electrons. With reference to a carefully measured experiment [99], an appropriate theoretical model for the crystal field which includes all $^{2S+1}L_J$ terms of the f^2 configuration of Pr^{3+} was deduced. The magnetic

M	$\mathbf{B} \parallel [1\ 0\ 0]$		$B \parallel [1\ 1\ 0]$	
	$ 0\rangle$	$ 1\rangle$	$ 0\rangle$	$ 1\rangle$
-4	-0.002	0.003	$0.002 - 0.002i$	$-0.002 - 0.002i$
-3	0.645	-0.663	$0.645i$	0.663
-2	-0.163	0.002	$-0.114 - 0.114i$	$-0.001 + 0.001i$
-1	0.205	0.211	0.205	$0.210i$
0	-0.002	0.0	0.0	$-0.001 - 0.001i$
1	0.205	-0.211	$0.205i$	0.210
2	-0.163	-0.002	$-0.114 - 0.114i$	$0.001 - 0.001i$
3	0.645	0.663	0.645	$0.663i$
4	-0.002	-0.003	$-0.002 + 0.002i$	$-0.002 - 0.002i$

Table 5.2: $|0\rangle$ is the calculated ground state and $|1\rangle$ is the first excited state $0.12meV$ above the ground for both \mathbf{B} field directions. At $T = 20K$ it is assumed that $|0\rangle$ and $|1\rangle$ are equally populated. The complete wave functions contain $\sim 10\%$ admixture of higher $^{2S+1}L_J$ terms, but only the components of the 3H_4 term are listed. The wave functions were calculated using a computer program written by Andrew Boothroyd and described in Ref. [99].

properties are found to be dominated by the ground state and 1st excited state. The wave functions of these states are given in table 5.2 with $\mathbf{B} \parallel [1\ 0\ 0]$ and $\mathbf{B} \parallel [1\ 1\ 0]$.

Once the wave function of Pr^{3+} is specified the magnetization density is obtained by calculating the expected value of appropriate magnetization density operators with respect to this wave function. Take the magnetization density spin and orbital operators to be [100]

$$\mathbf{M}^S(\mathbf{r}) = -2\mu_B \sum_{i=1}^n \mathbf{s}_i \delta(\mathbf{r} - \mathbf{r}_i) \quad (5.1)$$

and

$$\mathbf{M}^L(\mathbf{r}) = (1/[cr]) \int_r^\infty z \hat{\mathbf{r}} \times \mathbf{j}^L(z \hat{\mathbf{r}}) dz \quad , \quad (5.2)$$

where

$$\mathbf{j}^L(\mathbf{r}) = -(\mu_B c / \hbar) \sum_{i=1}^n [\mathbf{p}_i \delta(\mathbf{r} - \mathbf{r}_i) + \delta(\mathbf{r} - \mathbf{r}_i) \mathbf{p}_i] \quad . \quad (5.3)$$

\mathbf{r}_i , \mathbf{p}_i and \mathbf{s}_i are the position, momentum and spin of the i^{th} magnetic electron respectively, and $\hat{\mathbf{r}}$ is the unit vector of \mathbf{r} . With the operators in Eqs. (5.1-5.2) the relevant matrix elements can be written as [100]

$$\begin{aligned} \langle SLJM | M_q^S(\mathbf{r}) | S' L' J' M' \rangle &= -\frac{\mu_B}{\pi} \sum_{K, Q, K', Q'} Y_Q^K(\hat{\mathbf{r}}) U^2(r) (-1)^{\frac{1}{2}+M+q-J'+L'+S'} \\ &\times \sqrt{3/2} [l][K'] \sqrt{[K][S][S'][L][L'][J][J']} n \sum_{\bar{\theta}} (\theta \{ |\bar{\theta} \}) (\theta' \{ |\bar{\theta} \}) (-1)^{\bar{S}+\bar{L}} \\ &\times \left\{ \begin{matrix} S & 1 & S' \\ \frac{1}{2} & \bar{S} & \frac{1}{2} \end{matrix} \right\} \left\{ \begin{matrix} L & K & L' \\ l & \bar{L} & l \end{matrix} \right\} \left\{ \begin{matrix} 1 & K & K' \\ S' & L' & J' \\ S & L & J \end{matrix} \right\} \\ &\times \left(\begin{matrix} J & K' & J' \\ -M & Q' & M' \end{matrix} \right) \left(\begin{matrix} K & K' & 1 \\ Q & Q' & -q \end{matrix} \right) \left(\begin{matrix} l & K & l \\ 0 & 0 & 0 \end{matrix} \right) \end{aligned} \quad (5.4)$$

and

$$\begin{aligned} \langle SLJM | M_q^L(\mathbf{r}) | S' L' J' M' \rangle &= -\frac{\mu_B}{\pi} \sum_{K, Q, K', Q'} Y_Q^K(\hat{\mathbf{r}}) \frac{1}{r} \int_r^\infty U^2(z) dz \\ &\times (-1)^{q+M+L+L'+S} \delta_{SS'} [l]^{3/2} \sqrt{[J][J'][L][L'][K]l(l+1)[K']} \\ &\times \left(\begin{matrix} l & K & l \\ 0 & 0 & 0 \end{matrix} \right) \left\{ \begin{matrix} l & K' & l \\ K & l & 1 \end{matrix} \right\} \left\{ \begin{matrix} K' & L' & L \\ S & J & J' \end{matrix} \right\} n \sum_{\bar{\theta}} (\theta \{ |\bar{\theta} \}) (\theta' \{ |\bar{\theta} \}) (-1)^{\bar{L}} \\ &\times \left\{ \begin{matrix} K' & l & l \\ \bar{L} & L & L' \end{matrix} \right\} \left(\begin{matrix} J & K' & J' \\ -M & Q' & M' \end{matrix} \right) \left(\begin{matrix} K & K' & 1 \\ Q & Q' & -q \end{matrix} \right) \quad . \end{aligned} \quad (5.5)$$

The notation used in Eqs. (5.4-5.5) originates from atomic physics [101]. The 2×3 arrays with round and curly brackets are named $3j$ and $6j$ symbols respectively, and the 3×3 array in Eq. (5.4) is a $9j$ symbol. θ , θ' and $\bar{\theta}$ are shorthand for SL , $S'L'$ and $\bar{S}\bar{L}$ respectively, where θ and θ' are possible LS coupling terms (or Russell-Saunders terms) which can be formed from the l^n electronic configuration and $\bar{\theta}$ possible coupling terms formed from the l^{n-1} configuration (called parent terms); l is the orbital quantum number of the open ionic shell and n is the number of electrons in that shell. As an example, for Pr^{3+} , which has two $4f$

electrons, then $l = 3$ and $n = 2$ and since only one LS coupling term can be formed from a one electron configuration ($l^{n-1} = 3^1$), Pr^{3+} has only one parent term with $\bar{S} = 1/2$ and $\bar{L} = 3$ (in spectroscopic notation 2F). $(\theta\{|\bar{\theta}\})$ is a so-called coefficient of fractional percentage, see for instance Chap. 5, Sec. 6 of Ref. [101] for how to calculate such fractional percentage in general. For Pr^{3+} , which has only one parent term, the fractional percentage is simply $(\theta\{|\bar{\theta}\}) = 1$. Y_Q^K is the well-known spherical harmonic of rank K and order Q , and $U(r)$ is the radial wave function for an electron of the l^n configuration, assumed to be the same for all n electrons. For the calculation of the magnetization density of Pr^{3+} the radial wave function in Eq. (4.31), Sec., Chap. 4 is used. The total magnetization density at any point in space is clearly the sum of the spin and orbital magnetization density, i.e. $M_q = M_q^S + M_q^L$. The sub-index q of M_q^S and M_q^L refers to the spherical components and $q = 1, 0, -1$. These relate to cartesian vector components as follows $M_x = \frac{1}{\sqrt{2}}(M_{-1} - M_1)$, $M_y = \frac{1}{i\sqrt{2}}((M_{-1} + M_1))$ and $M_z = M_0$.

The expressions in Eqs. (5.4-5.5) may look complicated, but are relatively straight forward to derive, although this is somewhat painstaking to do. A number of authors have contributed to obtaining matrix expressions of this type. In this context, a theory suitable for relativistic calculations can be found in Ref. [102], and a general summary and introduction to these works can be found in Chap. 11 in Ref. [4].

Andrew Boothroyd and I have independently written computer programs for calculating the matrix elements $\langle\psi|M_i|\psi\rangle$, $i = x, y, z$, where $|\psi\rangle$ is a wave function from table 5.2. The calculation of the densities was carried out on a $65 \times 65 \times 65$ grid of a cubic box with length a (a being the lattice parameter a for $PrBa_2Cu_3O_{6.24}$). The grid point (n_x, n_y, n_z) , where n_x, n_y, n_z are any integers $0, 1 \dots 64$, is the center of a bin at $(n_x, n_y, n_z) \frac{a}{64}$ stretching from $\frac{n_x a}{64} - \frac{a}{2 \cdot 64}$ to $\frac{n_x a}{64} + \frac{a}{2 \cdot 64}$ along $i = x, y, z$. To make the comparison with experimental results easier the center of the Pr^{3+} density is positioned at $(\frac{a}{2}, \frac{a}{2}, \frac{a}{2})$ within the cubic

box. Since the orbital magnetization density diverges at $r = 0$, see Eq. (5.5), then special care need to be taken for obtaining a number representing the average density for the bin centered at $(\frac{a}{2}, \frac{a}{2}, \frac{a}{2})$ (in Eq. (5.5) at $r = 0$). For this purpose, notice that when integrating the spherical components of $\langle SLJM | \mathbf{M}(\mathbf{r}) | SLJM' \rangle$ over a sphere with radius r_0 we obtain

$$\begin{aligned} & \int_0^{r_0} \int_0^\pi \int_0^{2\pi} \langle SLJM | M_q(\mathbf{r}) | SLJM' \rangle r^2 dr d\Omega \\ &= \begin{cases} -\mu_B \tilde{g} M \delta_{MM'} & \text{for } q = 0 \\ -\mu_B \tilde{g}(-q) \frac{1}{\sqrt{2}} [(J - qM')(J + qM' + 1)]^{1/2} \delta_{M(M'+q)} & \text{for } q = -1, 1 \end{cases}, \end{aligned} \quad (5.6)$$

where

$$\tilde{g} = \int_0^{r_0} [r^2 U^2(r) + f(r) + (r^2 U^2(r) - f(r)) [S(S+1) - L(L+1)] / (J(J+1))] dr, \quad (5.7)$$

and $f(r) = r \int_r^\infty U^2(z) dz$. Hence, an average density for the bin centered at $(\frac{a}{2}, \frac{a}{2}, \frac{a}{2})$ is obtained separately using the expression in Eq. (5.6) with $r_0 = \frac{a}{2\sqrt{64}}$ (and divided by $(\frac{a}{64})^3$ to obtain a density). Notice, with $r_0 = \infty$ then \tilde{g} in Eq. (5.7) reduces to the expression for the well known Landé splitting factor for a paramagnetic ion⁴.

Consider first the wave function for Pr^{3+} calculated with the applied field $\mathbf{B} \parallel [1\ 0\ 0]$ in table 5.2. The component of $\langle \mathbf{M}(\mathbf{r}) \rangle_{[1\ 0\ 0]}$ ⁵pointing in the $[1\ 0\ 0]$ direction⁶ is drawn as two isosurfaces in Fig. 5.2(e-f). What is suggested perhaps unexpectedly, by the theoretical calculation is that the tetragonal crystal symmetry of $\text{PrBa}_2\text{Cu}_3\text{O}_{6.24}$ is broken by an applied \mathbf{B} field of $4.6T$. This is interesting because it stresses that the induced moment distribution in $\text{PrBa}_2\text{Cu}_3\text{O}_{6.24}$ with

⁴Use $\int_0^\infty r^2 U^2(r) dr = 1$ and $\int_0^\infty f(r) dr = \frac{1}{2}$ then $\tilde{g}(\infty) = \frac{3}{2} + \frac{1}{2} [S(S+1) - L(L+1)] / (J(J+1))$. $U(r)$ is the radial part of the orbital function. In atomic units the radial part of the density ρ in Eq. (4.31) is related to U as $\rho = U^2$.

⁵where $\langle \mathbf{M}(\mathbf{r}) \rangle$ is the thermal average $\langle \mathbf{M}(\mathbf{r}) \rangle = \frac{\langle 0 | \mathbf{M} | 0 \rangle + \langle 1 | \mathbf{M} | 1 \rangle}{2}$ due to $|0\rangle$ and $|1\rangle$ being equally populated, see caption table 5.2.

⁶The other two components have integrated moments of zero.

different applied field directions may be slightly or even considerably different. It is for this reason that the data measured for $\text{PrBa}_2\text{Cu}_3\text{O}_{6.24}$ are analysed as two separate data sets here, one data set for each \mathbf{B} -field orientation, before being analysed as an ‘averaged’ data set. Fig. 5.2(a-d) show the projection of $\langle M_x(\mathbf{r}) \rangle_{[1\ 0\ 0]}$ onto the plane $[0\ 1\ 0] - [0\ 0\ 1]$ in Sec. 5.4. It is the spatial distribution of the magnetization density perpendicular to the applied field that can be observed most directly by polarised neutron diffraction, see Chap. 1.

In Fig. 5.3(e-f) the component of $\langle \mathbf{M}(\mathbf{r}) \rangle_{[1\ 1\ 0]}$ parallel to $[1\ 1\ 0]$ is shown as two isosurfaces, where the thermal average $\langle \mathbf{M}(\mathbf{r}) \rangle_{[1\ 1\ 0]}$ is calculated using the wave functions given in table 5.2 (see also footnote 5). As for $\langle M_x(\mathbf{r}) \rangle_{[1\ 0\ 0]}$ the theoretical calculation predicts that the applied \mathbf{B} field breaks the tetragonal crystal symmetry. Otherwise, apart from being rotated by 45° , the calculated magnetization densities are quite similar, in particular when comparing the projected densities onto the plane perpendicular to the field direction.

5.3.2 Comparison with data

From the data measured with the applied field $\mathbf{B} \parallel [1\ 0\ 0]$ consider the structure factors in the $[0\ 1\ 0] - [0\ 0\ 1]$ plane. There are 52 of these in tables 5.5-5.6 and by adding the zero- q data point a data set consisting of 53 structure factors is generated. A reconstruction of this data set with⁷ $\bar{M}^s = 0.1\mu_B$ ($Q = P = 53$) on a 64×256 grid is shown in Fig. 5.4 for four different cut-off values. a and c are the lattice parameters along $[0\ 1\ 0]$ and $[0\ 0\ 1]$ and the plane crystal symmetry is mm (same symmetry as used for the thesis model in Sec. 4.4.2, Chap. 4). A cut-off value means the value above which all magnetization density values are set equal to this value. Using cut-off values helps emphasize structures at different magnetization density levels in Fig. 5.4. Separately, in Fig. 5.6(a) a contour plot of the magnetization density without cut-off for a part of the unit

⁷The \bar{M}^s value is obtained using the recipe in Sec. 4.7, Chap. 4, see also Fig. 5.9.

cell centered around the Pr site is shown. From this figure it is clear that at the highest contour levels the magnetization density of Pr is spherically distributed. A similar structure is observed from the crystal field calculation in Fig. 5.2(a) and comparing with Fig. 5.6(a) the only difference is a depletion of density at the center of the Pr density that is not observed experimentally. However, even if this feature was present it is probably not detected with the data in tables 5.5-5.6 because of its small spatial dimensions. Its spherical diameter is close to $\frac{a}{64}$, to reveal a structure of this scale it would require data with Miller indices of the order (32, 32, 96), this is beyond the data in tables 5.5-5.6 ⁸.

By comparing Fig. 5.2(b) with Fig. 5.4(a), Fig. 5.2(c) with Fig. 5.4(b) and Fig. 5.2(d) with Fig. 5.4(c) a good comparison is seen between the shape and diameter of the calculated and experimentally obtained Pr density. This suggests that the theoretical model is adequate for describing the observed Pr density for density values ranging from the maximum density value to a factor of 100 or more below that value; only at this point does the observed Pr density start to show substantial derivations from the calculated density.

To obtain an idea of the significance of the individual features in Fig. 5.4(a-d), error estimates (standard derivations) are calculated using the covariance procedure outlined in Sec. 4.6, Chap. 4. These are listed in table 5.3 for the $[0\ 1\ 0] - [0\ 0\ 1]$ reconstruction. The feature listed first represents an integration of the corner densities, presumably originating from an induced moment on Cu(1). It is found to be of size $0.0109 \pm 0.0028 \mu_B$. Such a moment is small relative to the induced moment of the Pr ion, which is found to be $0.2492 \pm 0.0028 \mu_B$, but significant within the uncertainty of the data. Its slightly odd shape suggests that

⁸As a rule of thumb, a Miller index h may give structural information on interval length $\frac{a}{2h}$. This rule of thumb is a simplified version of the well-known sampling theorem in Fourier analysis (see e.g. [103] page 230) which states that any band width limited function where for all $|h| > h_{max}$, $F_h = 0$ then the function in real space is fully defined by sampling at points with the interval equal to $\frac{a}{2h}$.

description of feature	position [Å]	area of integration [0 1 0] [a] [0 0 1] [c]		multi- plicity	moment \pm s.d. [μ_B]
Cu(1)	(0, 0)	$-\frac{13}{64} : \frac{13}{64}$	$-\frac{29}{256} : \frac{29}{256}$	1	0.0109 ± 0.0028
Pr	$(\frac{a}{2}, \frac{c}{2})$	$\frac{17}{64} : \frac{47}{64}$	$\frac{107}{256} : \frac{149}{256}$	1	0.2492 ± 0.0028
Pr on Ba site	$(\frac{a}{2}, 2.5)$	$\frac{21}{64} : \frac{43}{64}$	$\frac{43}{256} : \frac{73}{256}$	2	0.0164 ± 0.0032
probably Pr (or O(2))	$(\frac{a}{2}, 4.1)$	$\frac{25}{64} : \frac{39}{64}$	$\frac{77}{256} : \frac{97}{256}$	2	0.0021 ± 0.0014
negative feature	$(\frac{a}{2}, 0)$	$\frac{19}{64} : \frac{45}{64}$	$-\frac{19}{256} : \frac{19}{256}$	1	-0.0103 ± 0.0027
negative feature	(0.5, 2.0)	$\frac{1}{64} : \frac{21}{64}$	$\frac{33}{256} : \frac{57}{256}$	4	-0.0034 ± 0.0014
left/right of Pr	$(0, \frac{c}{2})$	$-\frac{9}{64} : \frac{9}{64}$	$\frac{111}{256} : \frac{145}{256}$	1	0.0036 ± 0.0020

Table 5.3: Summed moments over bins of the $[0\ 1\ 0] - [0\ 0\ 1]$ reconstruction in Fig. 5.4. The area of integration defines the area which is summed over, and a and c are the refined lattice constants for $\text{PrBa}_2\text{Cu}_3\text{O}_{6.24}$ (see table 5.1). The multiplicity, calculated moment and standard deviation in the reconstruction of each integrated feature is listed in columns 4 and 5.

description of feature	position [Å]	area of integration [-1 1 0] [$\frac{a}{\sqrt{2}}$] [0 0 1] [c]		multi- plicity	moment \pm s.d. [μ_B]
Pr	$(\frac{a}{\sqrt{2}}, \frac{c}{2})$	$\frac{15}{64} : \frac{49}{64}$	$\frac{107}{256} : \frac{149}{256}$	1	0.2530 ± 0.0030
Pr on Ba site	$(\frac{a}{\sqrt{2}}, 2.5)$	$\frac{19}{64} : \frac{45}{64}$	$\frac{41}{256} : \frac{69}{256}$	2	0.0109 ± 0.0025
probably Pr (or Cu(2))	$(\frac{a}{\sqrt{2}}, 3.8)$	$\frac{23}{64} : \frac{41}{64}$	$\frac{73}{256} : \frac{87}{256}$	2	0.0020 ± 0.0013
negative feature	$(\frac{a}{2\sqrt{2}}, 2.1)$	$-\frac{13}{64} : \frac{13}{64}$	$\frac{37}{256} : \frac{55}{256}$	2	-0.0030 ± 0.0016
negative feature	$(\frac{a}{2\sqrt{2}}, 5.1)$	$-\frac{9}{64} : \frac{9}{64}$	$\frac{103}{256} : \frac{121}{256}$	2	-0.0012 ± 0.0012
left/right of Pr	$(\frac{a}{2\sqrt{2}}, \frac{c}{2})$	$-\frac{5}{64} : \frac{5}{64}$	$\frac{125}{256} : \frac{131}{256}$	1	0.0003 ± 0.0008
‘deformation’ of Pr	(3.4, 4.8)	$\frac{41}{64} : \frac{51}{64}$	$\frac{99}{256} : \frac{107}{256}$	4	0.0001 ± 0.0004

Table 5.4: Summed moments over bins of the $[-1\ 1\ 0] - [0\ 0\ 1]$ reconstruction in Fig. 5.5

there may be an induced moment other than the Cu(1) moment contributing to this feature. This Cu(1) moment may be compared to induced moments for the same site in isostructural $\text{YBa}_2\text{Cu}_3\text{O}_{6+x}$. A number of PND experiments have been carried out on $\text{YBa}_2\text{Cu}_3\text{O}_{6+x}$ for a variety of different oxygen compositions, applied \mathbf{B} fields and temperatures [74],[104],[105],[106],[107],[108]. However, a direct comparison to these works is difficult because the induced magnetic moments in $\text{YBa}_2\text{Cu}_3\text{O}_{6+x}$ show a strong temperature dependence [74] and variation with oxygen composition⁹. One notable difference, though, is that the Cu(1) moment is between a factor of 2 to 10 times larger here, than in these references.

The largest feature not situated at the Pr site has its center at $\sim (\frac{a}{2}, 2.5\text{\AA})$, see Fig. 5.2(a-c), close to the Ba nuclear position $(\frac{a}{2}, 0.19171 \cdot c \simeq 2.3\text{\AA})$ as determined from the unpolarised neutron diffraction experiment (see table 5.1). Since Ba is non-magnetic the feature centered at $(\frac{a}{2}, 2.5\text{\AA})$ cannot be explained by an induced moment originating from Ba. Instead it is evidence of Ba/Pr cation mixing, it shows the moment from the small fraction of Pr ions which have been substituted for Ba ions on the Ba site in the $\text{PrBa}_2\text{Cu}_3\text{O}_{6.24}$ single crystal used for our neutron experiments. From table 5.3 this moment is found to be $0.0164 \pm 0.0032\mu_B$, which is 6% of the Pr moment and is only an estimate taking into consideration that the susceptibility of Pr on the Ba site may not be the same as Pr on the Pr site. A nearby feature with center $\sim (\frac{a}{2}, 4.1\text{\AA})$ and moment $0.0021 \pm 0.0014\mu_B$ may also be originating from an induced moment on a tiny number of interstitial Pr ions on this site. Alternatively its position is near the O(2) nuclear site $(\frac{a}{2}, 0.3697 \cdot c = 4.4\text{\AA})$ hence it could be attributed to O(2).

A number of relatively strong negative features are present. The largest of these is positioned at $(\frac{a}{2}, 0)$, see Fig. 5.4(d), with moment $-0.0103 \pm 0.0027\mu_B$.

⁹In Ref. [106] it is argued that two crystals with the same oxygen composition held at the same temperature may also exhibit different Cu(1) moments due to specific oxygen ordering of each sample, depending on how the samples were prepared.

An obvious guess would be that this feature originates from an induced moment on the O(3) atom position at the crystallographic site $(1/2, 0, 0)$. However, later discussion suggests that it may be situated at the $(1/2, 1/2, 0)$ crystallographic site, or alternatively a combination of both $(1/2, 0, 0)$ and $(1/2, 1/2, 0)$. More importantly, this feature is definitely real within the uncertainty of the data. Close to $(0.5\text{\AA}, 2.0\text{\AA})$ in Fig. 5.4(d) is a smaller negative moment of $-0.0034 \pm 0.0014\mu_B$. Its multiplicity in the $[0\ 1\ 0] - [0\ 0\ 1]$ reconstruction is 4 and therefore its total moment contribution to the unit cell is $4(-0.0034\mu_B) = -0.0136\mu_B$, and it will be discussed in some detail later. The last feature of table 5.3 is situated to the left and right of the Pr site with a moment of $0.0036 \pm 0.0020\mu_B$. It is quite a small moment and its origin is unknown.

The second independent data set to be discussed is obtained by selecting those structure factors measured with $\mathbf{B} \parallel [1\ 1\ 0]$ and with Miller indices in the $[-1\ 1\ 0] - [0\ 0\ 1]$ plane. There are 36 of those in tables 5.5-5.6 and by adding the zero- q structure factor a data set consisting of 37 structure factors is obtained. A MEMx reconstruction of this data set with $\bar{M}^s = 0.1\mu_B$ ($Q = P = 37$) is shown in Fig. 5.5 and Fig. 5.6(b). The data are contained in the $[-1\ 1\ 0] - [0\ 0\ 1]$ plane, so the periodic lattice parameters are $\frac{a}{\sqrt{2}}$ and c respectively, and for convenience the $[-1\ 1\ 0]$ axis is displayed from $\frac{a}{2\sqrt{2}}$ to $\frac{3a}{2\sqrt{2}}$. As for the $[0\ 1\ 0] - [0\ 0\ 1]$ reconstruction the plane symmetry is mm and the reconstruction is calculated on a 64×256 grid.

For the highest magnetization density values the experimentally obtained density around the Pr site in Fig. 5.6(b) takes the form of a sphere, in agreement with the theoretical calculated density in Fig. 5.5(a)¹⁰. This agrees with observations made for the $[0\ 1\ 0] - [0\ 0\ 1]$ reconstruction and confirms that, with the available data and at the strongest magnetization density levels, the Pr density

¹⁰Except for fine features in the theoretical density not present in the experimental observed density. Even if these are present they are not expected to be revealed with the available data, because of their small spatial dimension - see discussion of Fig. 5.6(a) in the text above.

shows no evidence of deviating from the crystal field calculated density. For magnetization density values a factor of 100 or more lower than the highest density value there is evidence of small ‘deformations’ of the Pr density from, the shape predicted by the crystal field calculations. Of these deformations only one seems to be pointing in the direction of one of the known nuclear sites (other than the Pr site) as determined from the unpolarised neutron experiment (see table 5.1). This feature is most clearly seen in Fig. 5.5(c) close to $(3.4\text{\AA}, 4.8\text{\AA})$ and could possibly be pointing towards the O(2) nuclear positions at $(0, 4.4\text{\AA})$. It is relatively small in magnitude compared to the majority of other features in the reconstruction and an attempt to integrate over it¹¹ gave $0.0001 \pm 0.0004\mu_B$. To the left and right of the Pr site in Fig. 5.5(b-c) is another small feature with $0.0003 \pm 0.0008\mu_B$, this is also weak. Another structure close to the Pr site is the negative feature at $\sim (\frac{a}{2\sqrt{2}}, 5.1\text{\AA})$ with $-0.0012 \pm 0.0012\mu_B$ (see Fig. 5.5(d)), and is just about significant within the uncertainty of the data. The strongest negative moment for the $[-1\ 1\ 0] - [0\ 0\ 1]$ reconstruction appears at $\sim (\frac{a}{2\sqrt{2}}, 2.1\text{\AA})$ with $-0.0030 \pm 0.0016\mu_B$. Combined with the observed negative features for the $[0\ 1\ 0] - [0\ 0\ 1]$ reconstruction, see Fig. 5.4(d), the strongest negative features appear to be in and below the region of the Ba site (as seen from the bottom Ba site). Apart from the moment on the Pr site, some of these contribute with some of the biggest moments in the unit cell, for instance the $(\frac{a}{2}, 0)$ and $(0.5, 2.0)$ features in the $[0\ 1\ 0] - [0\ 0\ 1]$ projection with total moments of $1 \times (-0.0103)\mu_B$ and $4 \times (-0.0034) = -0.0136\mu_B$ respectively. Under the assumption that the induced moments are distributed equally with $\mathbf{B} \parallel [1\ 0\ 0]$ and with $\mathbf{B} \parallel [1\ 1\ 0]$, the observation of smaller negative moments for the $[-1\ 1\ 0] - [0\ 0\ 1]$ projection may be explained in the region $z \simeq 0$ by a concentration of negative density close to the crystallographic site $(1/2, 1/2, 0)$ which could be cancelled out by a positive Cu(1) moment when projecting onto $[-1\ 1\ 0] - [0\ 0\ 1]$. Similarly, for $z \simeq 2\text{\AA}$, a

¹¹Because it is not located at an isolated position but is part of a larger feature it is difficult to determine the area which is covered i.e. its area of integration in table 5.4.

concentration close to the O(1) nuclear site may cancel out parts of the positive density at the Ba site, originating from Pr/Ba cation mixing. This latter feature is estimated to be $0.0109 \pm 0.0025\mu_B$ in the $[-1\ 1\ 0] - [0\ 0\ 1]$ reconstruction, this is $0.0060\mu_B$ less than the same feature in the $[0\ 1\ 0] - [0\ 0\ 1]$ projection, and supports the explanation of a negative moment close to the O(1) site. The moment at the Pr site is found to be $0.2530 \pm 0.0030\mu_B$ in the $[-1\ 1\ 0] - [0\ 0\ 1]$ reconstruction, this is within the experimental error of the value for the same feature in the $[0\ 1\ 0] - [0\ 0\ 1]$ reconstruction. The remaining feature listed in table 5.4 is located at $\sim (\frac{a}{\sqrt{2}}, 3.8\text{\AA})$ with $0.0020 \pm 0.0013\mu_B$. This feature together with the $(\frac{a}{2}, 4.1\text{\AA})$ feature in table 5.3 may be evidence of a small fraction of Pr ions close to the crystallographic site $(a/2, a/2, 4\text{\AA})$. Alternatively, the nuclear position of Cu(2) in the $[-1\ 1\ 0] - [0\ 0\ 1]$ projection is $(\frac{a}{\sqrt{2}}, \sim 4.2\text{\AA})$ and the $(\frac{a}{2}, 4.1\text{\AA})$ feature could be originating from Cu(2).

5.4 Reconstruction of ‘averaged’ $\text{PrBa}_2\text{Cu}_3\text{O}_{6.24}$ data set

In this section all the 91 structure factors in table 5.5 and the 13 ‘averaged’ structure factors in table 5.6 are considered as one data set. Adding the zero- q structure factor generates a data set consisting of 105 data points. In combining the data in tables 5.5-5.6 the assumption is (as also discussed in Sec. 5.2) that the induced moment distributions with $\mathbf{B} \parallel [1\ 0\ 0]$ and $\mathbf{B} \parallel [1\ 1\ 0]$ are very similar and the combined data set is analysed in space group $P4/\text{mmm}$, the known space group for $\text{PrBa}_2\text{Cu}_3\text{O}_{6.24}$. The extent to which this assumption is valid is difficult to assess, but judging from *i)* the similarity of the 13 structure factors in table 5.6 measured independently for both \mathbf{B} field orientations (compare $F_{hkl}^{B \parallel [1\ 0\ 0]} \pm \sigma_{hkl}^{B \parallel [1\ 0\ 0]}$ and $F_{hkl}^{B \parallel [1\ 1\ 0]} \pm \sigma_{hkl}^{B \parallel [1\ 1\ 0]}$ in table 5.6); *ii)* the similarities between the reconstructions in Fig. 5.4 and Fig. 5.5; and *iii)* the fact

that $\text{PrBa}_2\text{Cu}_3\text{O}_{6.24}$ has tetragonal symmetry which means that an applied \mathbf{B} field with any direction within the xy -plane is expected to induce the same total moment, the moment distributions with $\mathbf{B} \parallel [1\ 0\ 0]$ and $\mathbf{B} \parallel [1\ 1\ 0]$ are expected to be at least reasonably similar. It is therefore valid to analyse the combined data set. The data is reconstructed on a $16 \times 16 \times 64$ grid and the prior model constant \bar{M}^s is found using the recipe in Sec. 4.7, Chap. 4. To illustrate the latter, a FOM_1 versus \bar{M}^s plot is shown in Fig. 5.9, where the \bar{M}^s reference point is found to be $\bar{M}^s_{ref} \simeq 0.4\mu_B$ and therefore a \bar{M}^s value close to $0.1\mu_B$ is selected. Shown in Fig. 5.7 and continuing in Fig. 5.8 are 9 isosurfaces of the resulting reconstruction.

Starting from the top left-hand frame in Fig. 5.7, the isosurface at the contour level (CL) $1\mu_B\text{\AA}^{-3}$ is shown. This value is close to the highest magnetization density value, which is $3.08\mu_B\text{\AA}^{-3}$, and at this level, as expected, a single isosurface centered at the Pr site is observed. Moving down in contour levels the diameter of the isosurface enclosing the Pr site increases and at $\text{CL} = 0.05\mu_B\text{\AA}^{-3}$ the first feature not centered at the Pr site is seen. At $\text{CL} = 0.0025\mu_B\text{\AA}^{-3}$ a number of additional moments have appeared. All of these have been discussed in the previous section, but the isosurfaces offer additional information about the more precise spatial location in the unit cell, under the assumption that the induced moment distributions are very similar with the two \mathbf{B} field orientations. For instance it is seen from the $\text{CL} = 0.0025\mu_B\text{\AA}^{-3}$ isosurface that the negative density in the plane $z \simeq 0$ seems to be centered at $(1/2, 1/2, 0)$ stretching towards the Ba site. The last two isosurface plots in Fig. 5.8 show the $\text{CL} = 0.00075\mu_B\text{\AA}^{-3}$ isosurface from two different perspectives. $0.00075\mu_B\text{\AA}^{-3}$ is more than a factor of 1000 below the highest magnetization density value and at this level many new features appear which are not supported within the uncertainty of the data. However, none of the isosurfaces show any evidence of the density surrounding the Pr site pointing towards any known nuclear positions, including nuclear sites within the CuO_2 planes. Only at $\text{CL} = 0.001\mu_B\text{\AA}^{-3}$ does the Pr density start to

deviate from a spherical symmetric form, here it appears to be stretching towards the $(0, 0, 1/2)$ crystallographic site, which is unexpected as there are no known atoms located at this site.

5.5 Polarised neutron diffraction data from $\text{PrBa}_2\text{Cu}_3\text{O}_7$

One other PND experiment on $\text{PrBa}_2\text{Cu}_3\text{O}_{6+x}$ has been carried out [109], this used a single crystal of $\text{PrBa}_2\text{Cu}_3\text{O}_7$. It would be interesting to compare the magnetization densities of $\text{PrBa}_2\text{Cu}_3\text{O}_7$ and $\text{PrBa}_2\text{Cu}_3\text{O}_{6.24}$. To achieve the best conditions for such a comparison the sub-sets of data from both data sets with common Miller indices are used. For $\text{PrBa}_2\text{Cu}_3\text{O}_7$ this subset is taken from Ref. [110], and both data subsets contain 30 structure factors which are listed for $\text{PrBa}_2\text{Cu}_3\text{O}_7$ in table 5.7¹². The reconstruction for the $\text{PrBa}_2\text{Cu}_3\text{O}_{6.24}$ subset with $\bar{M}^s = 0.1\mu_B$ (as used previously), on a 64×256 grid, yields a total calculated moment of $0.2265\mu_B$, and is displayed in Fig. 5.10. The reconstruction for $\text{PrBa}_2\text{Cu}_3\text{O}_7$ using the same grid and prior model constants yields a total calculated moment of $0.3223\mu_B$, it is scaled down by a factor $\frac{0.2265}{0.3223}$ to allow better comparison between the two data set, and is displayed in Fig. 5.11. There are differences between the two magnetization density maps in Fig. 5.10 and Fig. 5.11. However, around the area of the Pr site there is striking similarity for both positive and negative magnetization density values. This shows that the overall structure of the magnetization density distribution in the neighbourhood of the Pr site has little dependence on the oxygen content in $\text{PrBa}_2\text{Cu}_3\text{O}_{6+x}$ (at least when going from $x = 1$ to $x = 0.24$). This might not be surprising considering that the Pr site is furthest away from the Cu(1)-O(3) chains in the unit cell, where oxygen atoms can be taken out or inserted into the structure. Probably the most significant difference between the two $\text{PrBa}_2\text{Cu}_3\text{O}_{6+x}$ compounds is seen at the Cu(1) position, where a stronger moment is induced on Cu(1) in $\text{PrBa}_2\text{Cu}_3\text{O}_7$

¹²The equivalent sub-set for $\text{PrBa}_2\text{Cu}_3\text{O}_{6.24}$ can be obtained from tables 5.5-5.6.

relative to Cu(1) in $\text{PrBa}_2\text{Cu}_3\text{O}_{6.24}$. The magnetization density near the Ba site is also different. These differences may be caused by the use of single crystals grown in different crucibles. To grow the $\text{PrBa}_2\text{Cu}_3\text{O}_7$ and $\text{PrBa}_2\text{Cu}_3\text{O}_{6.24}$ single crystals, Al_2O_3 and MgO crucible were used respectively.

Another issue governs the interpretation of regions of a magnetization density image which have zero density. This may seem trivial but it is worth a discussion in the context of data presented in this chapter. Clearly the question is only relevant when dealing incomplete data, as is usually the case, and the question of whether an area of zero density means that there is nothing there, or whether the zero density is caused by a shortcoming of the data may arise. As a first example, the sub-set containing the 30 data points used to generate Fig. 5.10 is taken from the larger 37 point data set discussed in Sec. 5.3.2 and displayed in Fig. 5.5. By comparing Fig. 5.10 and Fig. 5.5 it is clear that notable differences are present. Looking more carefully at these figures it is also apparent that there are no features in Fig. 5.10 which are not seen in some form in Fig. 5.5. The opposite is not the case, as expected. This emphasizes that when data are taken out of the data set the picture of the resulting reconstruction may change. More specifically, compare the Pr density in Fig. 5.10 and Fig. 5.5. From Fig. 5.10 the Pr density looks perfectly circular. However, the reconstruction in Fig. 5.5 is circular but with a few additional small features.

For the special case of going from Fig. 5.5 to Fig. 5.10 most of the information lost can be regained by simply adding two of the seven structure factors which are not part of the 30 point sub-set. This is illustrated in Fig. 5.12 where the $0\ 0\ 1$ and $0\ 0\ 2$ structure factors have been inserted back to obtain a 32 structure factor sub-set. It is therefore tempting to conclude that if the $0\ 0\ 1$ and $0\ 0\ 2$ structure factor were measured for the $\text{PrBa}_2\text{Cu}_3\text{O}_7$ crystal a similar re-distribution of the negative and positive magnetization would be observed.

5.6 Discussion and conclusions

Studying the magnetization density reconstructions of $\text{PrBa}_2\text{Cu}_3\text{O}_{6.24}$ in Sec. 5.3-5.4 and comparing then with the magnetization density of $\text{PrBa}_2\text{Cu}_3\text{O}_7$ in Sec. 5.5, a number of very interesting features are revealed, in many cases the evidence of these features in the data is great. How do these new observations relate to previous experimental and theoretical work?

Focusing on the induced moment density of the Pr ion, it was seen in Sec. 5.3 that its overall geometry (spherical) and size could be explained with a local crystal field model for Pr^{3+} . This is not surprising since a number of magnetic excitation spectra on $\text{PrBa}_2\text{Cu}_3\text{O}_{6+x}$ have been measured [111],[112],[99],[113],[114], and although the excitation spectra shown unusual peak broadening as compared to spectra measured on $R\text{Ba}_2\text{Cu}_3\text{O}_{6+x}$ (R =rare earth), the crystal field parameters describing the local environment of the Pr ion can be refined with good accuracy. Hence it is not surprising that the major shape of the induced Pr moment in $\text{PrBa}_2\text{Cu}_3\text{O}_{6.24}$ was found to be well described within such a crystal field model. However, crystal field parameters do not describe every detail of a rare earth local environment, for instance, effects which cause peak broadening are not accounted for. In particular the enhanced widths in the magnetic excitation spectrum of $\text{PrBa}_2\text{Cu}_3\text{O}_{6+x}$ are attributed to an increased hybridisation between $4f$ electrons and electronic states in the CuO_2 planes [111],[112],[99],[113], and such an hybridisation is said to be responsible for the T_C suppression in $\text{PrBa}_2\text{Cu}_3\text{O}_{6+x}$ by the majority of people working in this field (see review papers Refs. [1],[93] and references therein). It would therefore be of key interest if the structure of this hybridisation could be mapped out. A number of theoretical works, including Fehrenbacher & Rice model [94], predict the cause to involve a hybridisation of the $4f$ electrons of Pr and electronic states in the CuO_2 planes. An ideal experiment to perform in order to probe the exact spatial distribution of these $4f$ electrons is a PND experiment. This measures the Fourier components of the

magnetization density distribution in the unit cell and since only the $4f$ electrons of Pr are magnetic, it is only these Pr electrons which are detectable in a PND experiment, plus other non Pr magnetic contributions. A unit cell magnetization density may look different from a unit cell electron density (see Chap. 1), but a \mathbf{B} field of magnitude $4.6T$ was used for the PND experiments reported here and these densities should be similar. In any case, to make a direct comparison to a PND experiment the expectation value of magnetization density operators may be calculated for any proposed theoretical model and then compared directly with the observed magnetization density image.

In summary the following has been observed.

1. In the region around the Pr site the magnetization density distribution was
 - (a) found to be more or less independent of oxygen composition (at least when going from $x = 1$ to $x = 0.24$ for $\text{PrBa}_2\text{Cu}_3\text{O}_{6+x}$).
 - (b) The crystal field model refined from magnetic excitation spectra was found to describe the features of the Pr density for magnetization density values ranging from the highest value to $1/100$ of the highest value. However, from the discussions in Sec. 5.5 it should be remembered that if more structure factors are measured, the Pr density may gain more fine structure, although, the dominating Pr feature will remain the same.
 - (c) Small deviations of this density were seen below $1/100$, this puts a constraint on the degree of possible hybridisation and theoretical models like that of Fehrenbacher & Rice. In principle to make a full comparison would require the calculation of the magnetization density corresponding to the Fehrenbacher & Rice state (and equivalent states from other theoretical works) under the influence of an applied field, at a temperature just above the Neel temperature of the Pr moments (say $T = 20K$).

2. The observed magnetic structure in the region around the Ba site is also of interest, since some of these features could be key to the explanation of the suppression of superconductivity in $\text{PrBa}_2\text{Cu}_3\text{O}_{6+x}$, or may even be the reason for such suppression. The experiment which would clarify this uniquely, would be a PND experiment, as described in Sec. 5.2, using a single crystal of $\text{PrBa}_2\text{Cu}_3\text{O}_{6+x}$ grown under special conditions [115],[116], where superconductivity in this compound has been achieved. If the magnetization density distribution in the region of the Pr site is different for such a single crystal¹³ then Pr on the Pr site does contribute to the suppression of superconductivity for a ‘standard’ $\text{PrBa}_2\text{Cu}_3\text{O}_{6+x}$ crystal. It could may also be possible that small amounts of Pr/Ba mixing trigger the Pr ions on the Pr sites to form a hybridisation state with $\text{O}(2p)$ levels in the CuO_2 ?

¹³The comparison would be best for crystal grown with an oxygen composition where $\text{PrBa}_2\text{Cu}_3\text{O}_{6+x}$ is in its tetragonal phase.

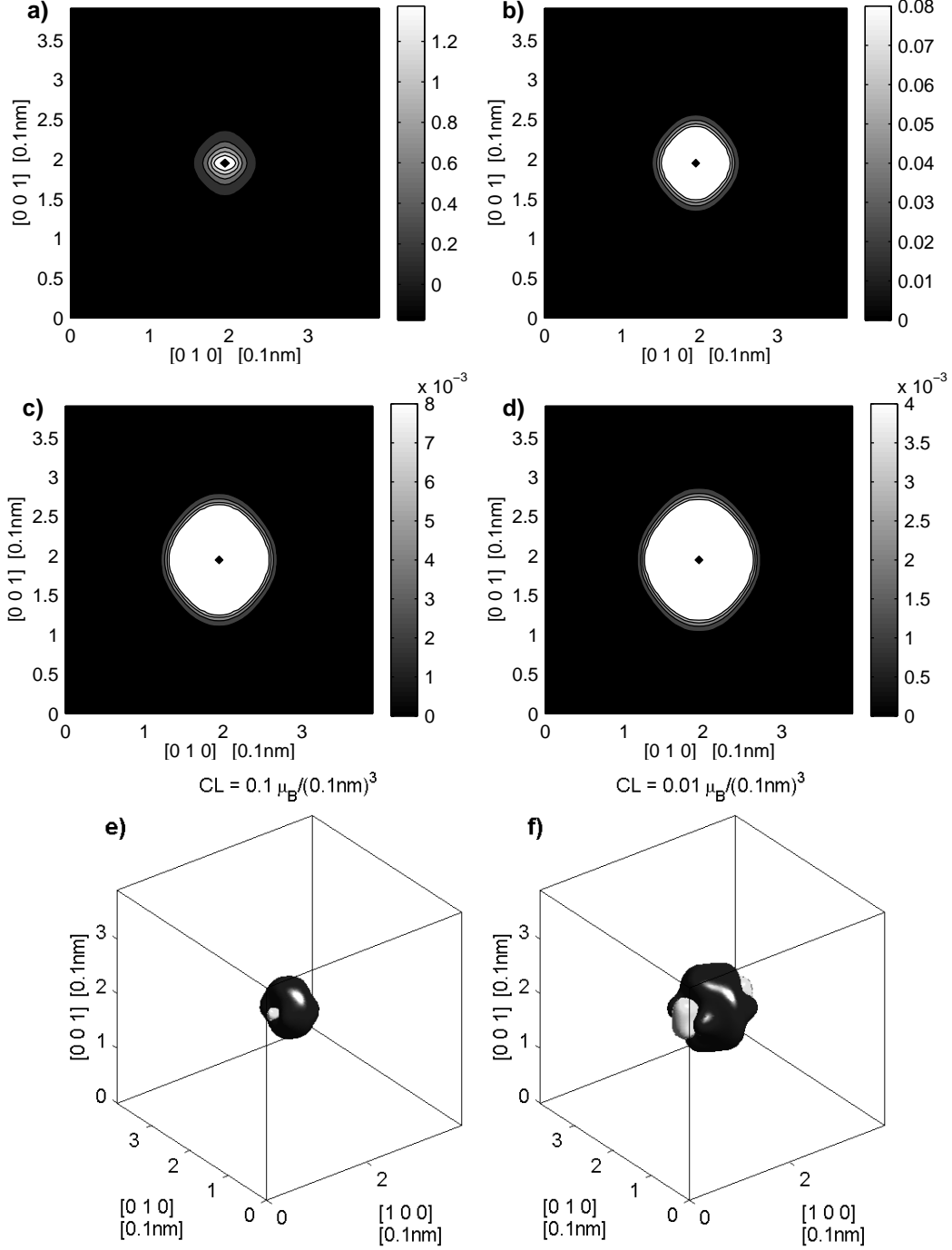


Figure 5.2: Shows $\langle M_x(\mathbf{r}) \rangle_{[1\ 0\ 0]}$. Two isosurfaces illustrate $\langle M_x \rangle$ in (e-f), the lighter coloured surfaces indicate negative magnetization of the same contour level. In (a-d) a projection of $\langle M_x \rangle$ is shown where in (b-d) all negative density = 0 and in addition in (b) all positive density above 0.1 is cut-off, in (c) cut-off=0.01 and in (d) $0.005 \mu_B \text{\AA}^{-2}$. 168

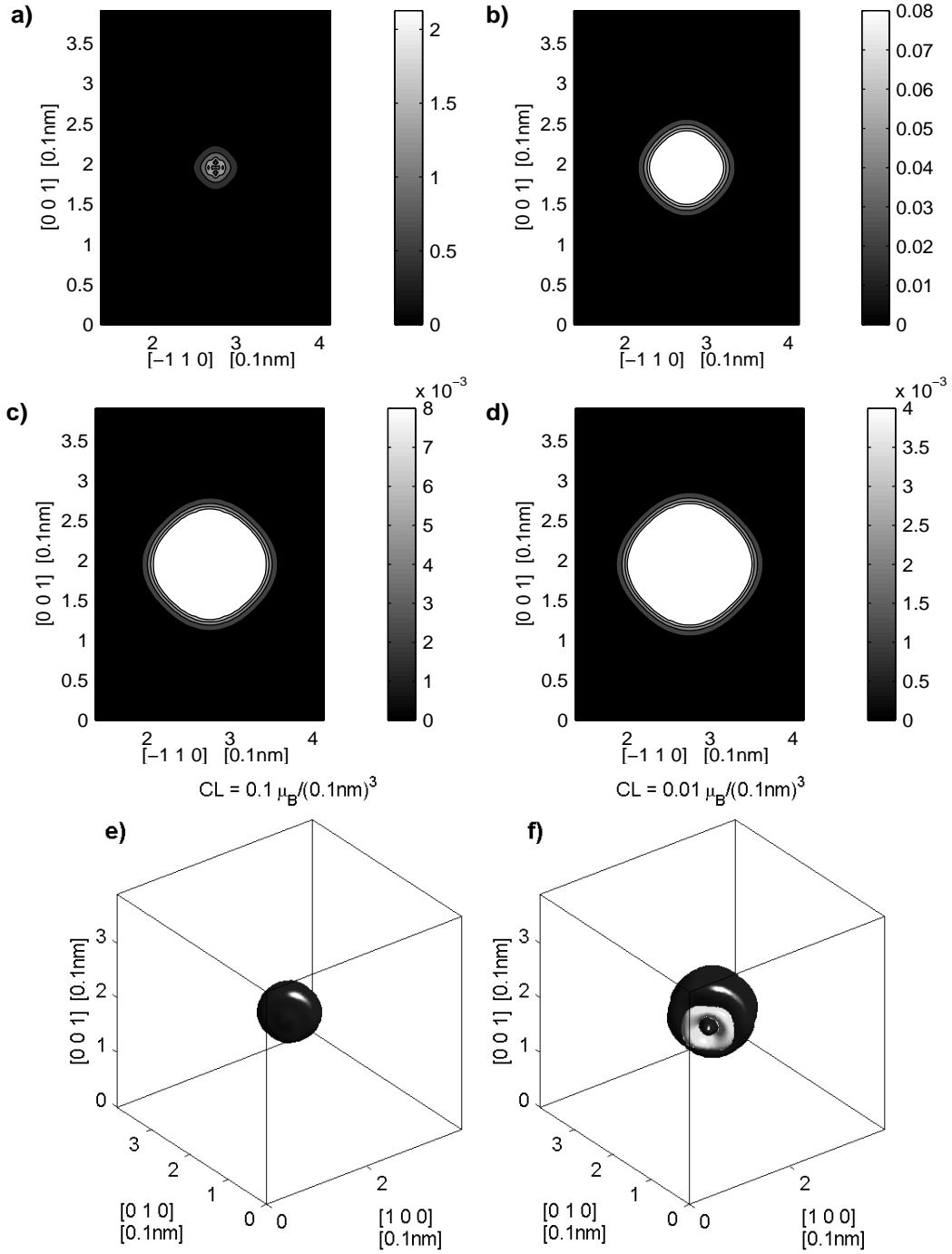


Figure 5.3: Same as in Fig. 5.2 but using the wave function with $\mathbf{B} \parallel [1\ 1\ 0]$ in table 5.2.

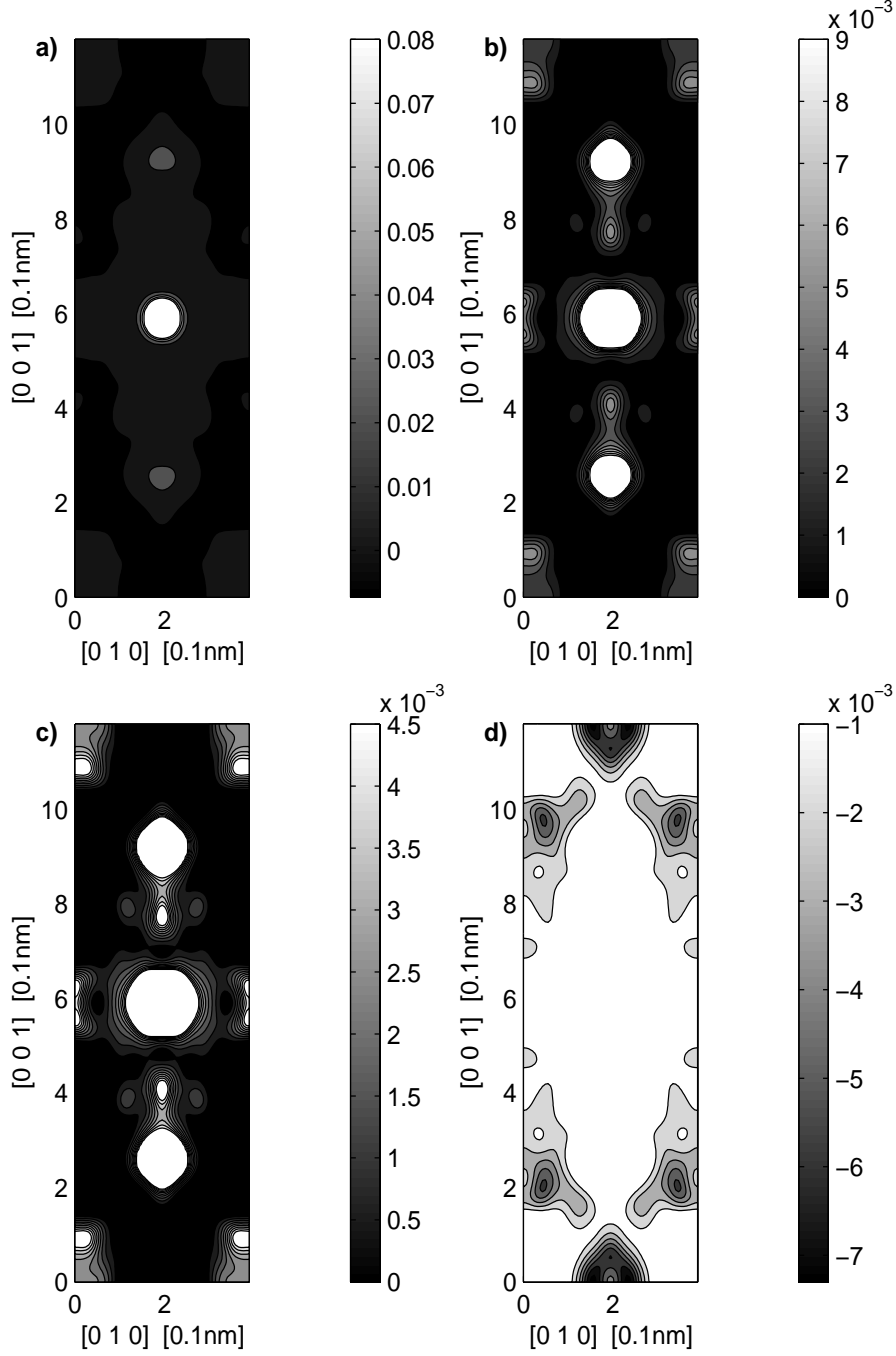


Figure 5.4: Shows a reconstruction of the data set consisting of the structure factors in tables 5.5-5.6 which are in the $[0\ 1\ 0] - [0\ 0\ 1]$ plane. In (a-d) all density above 0.1, 0.01, 0.005 and $0\mu\text{\AA}^{-2}$ respectively are cut-off. In addition in (b-c) all negative density = 0. $\bar{M}^s = 0.1\mu_B$ ($Q = P = 53$).

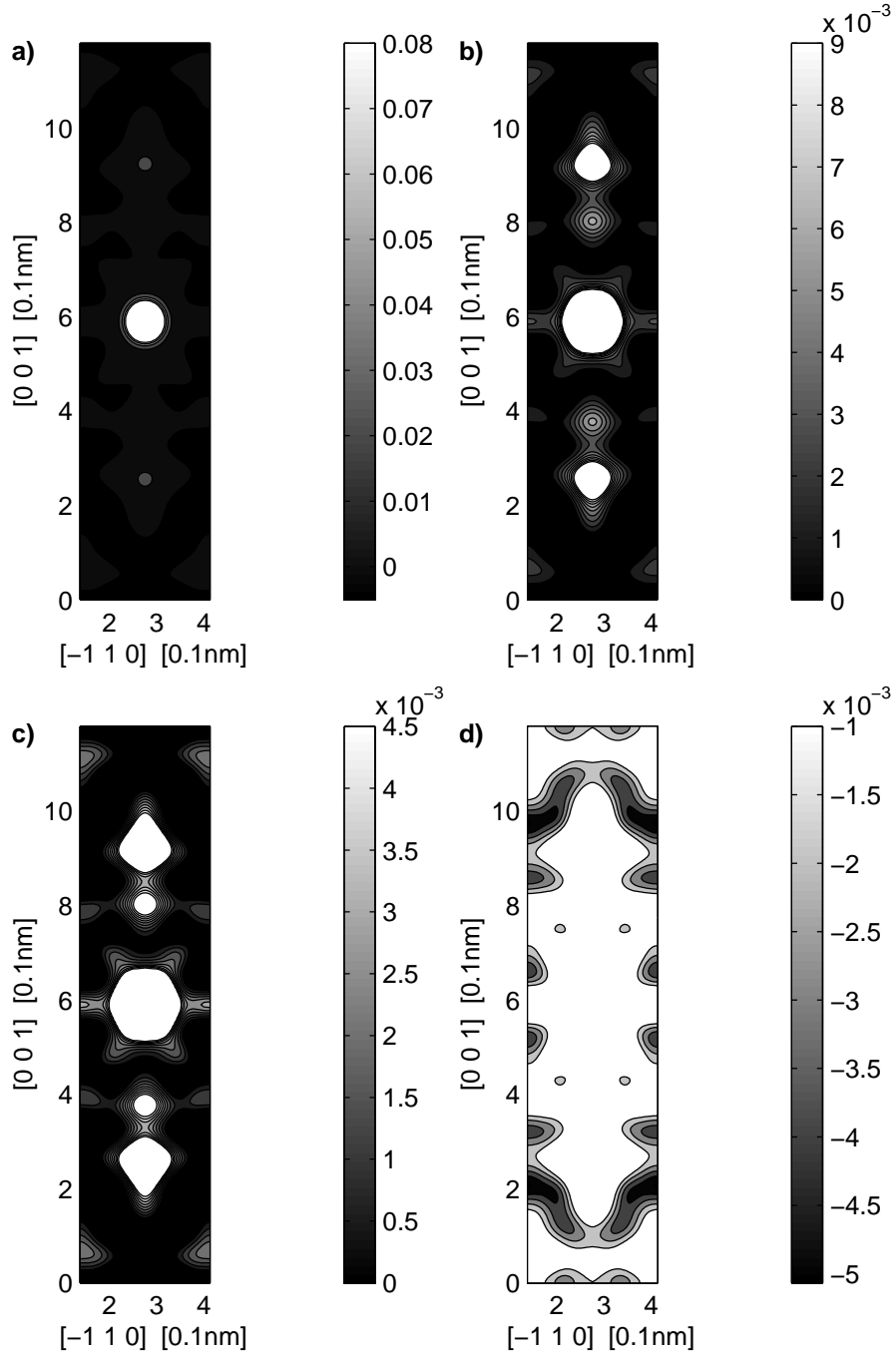


Figure 5.5: Same as in Fig. 5.4 but for the data in tables 5.5-5.6 which are in the $[1\ 1\ 0] - [0\ 0\ 1]$ plane. $\bar{M}^s = 0.1\mu_B$ ($Q = P = 37$).

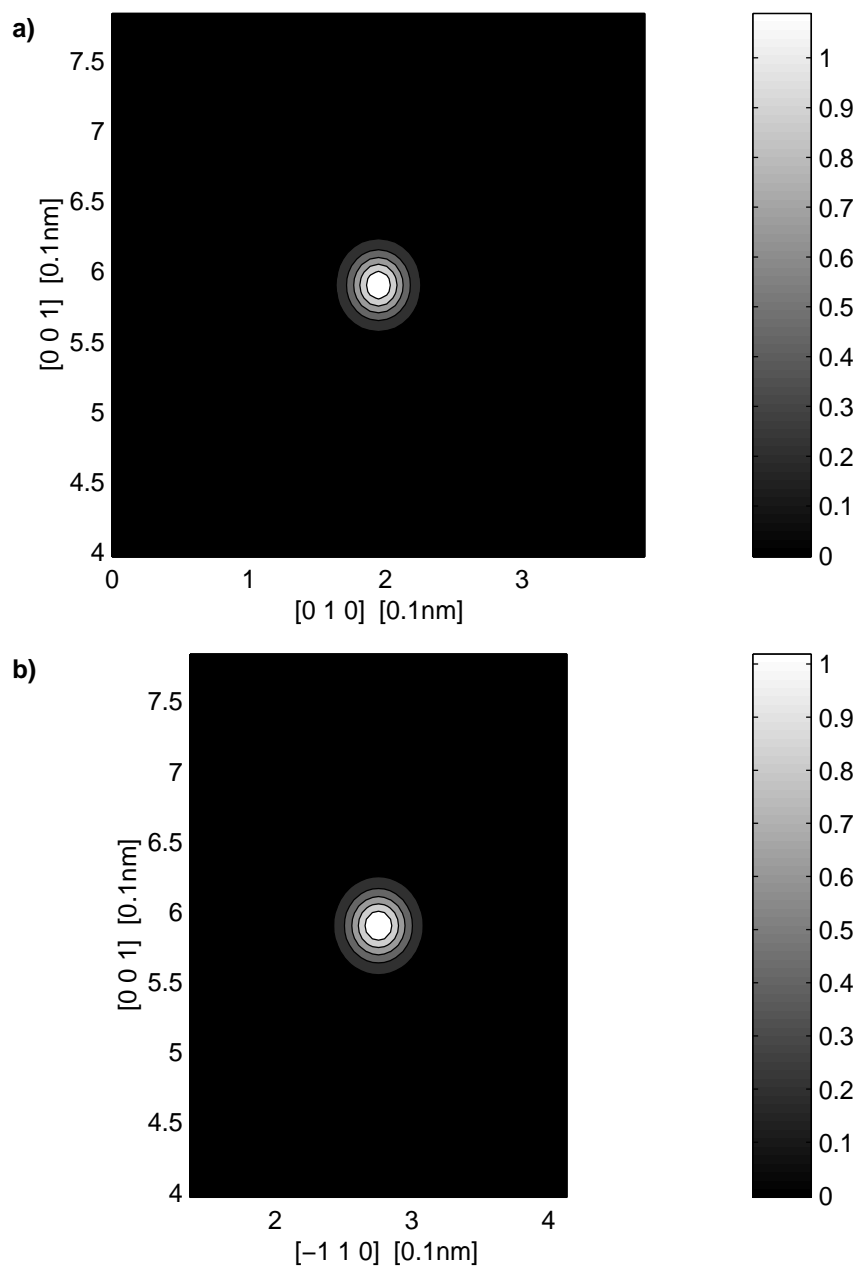


Figure 5.6: (a) same shows a contour plot of same reconstruction as described in Fig. 5.4 with no cut-off and for part of the unit to emphasize the density close to the Pr site. (b) same as (a) but for the reconstruction in Fig. 5.5.

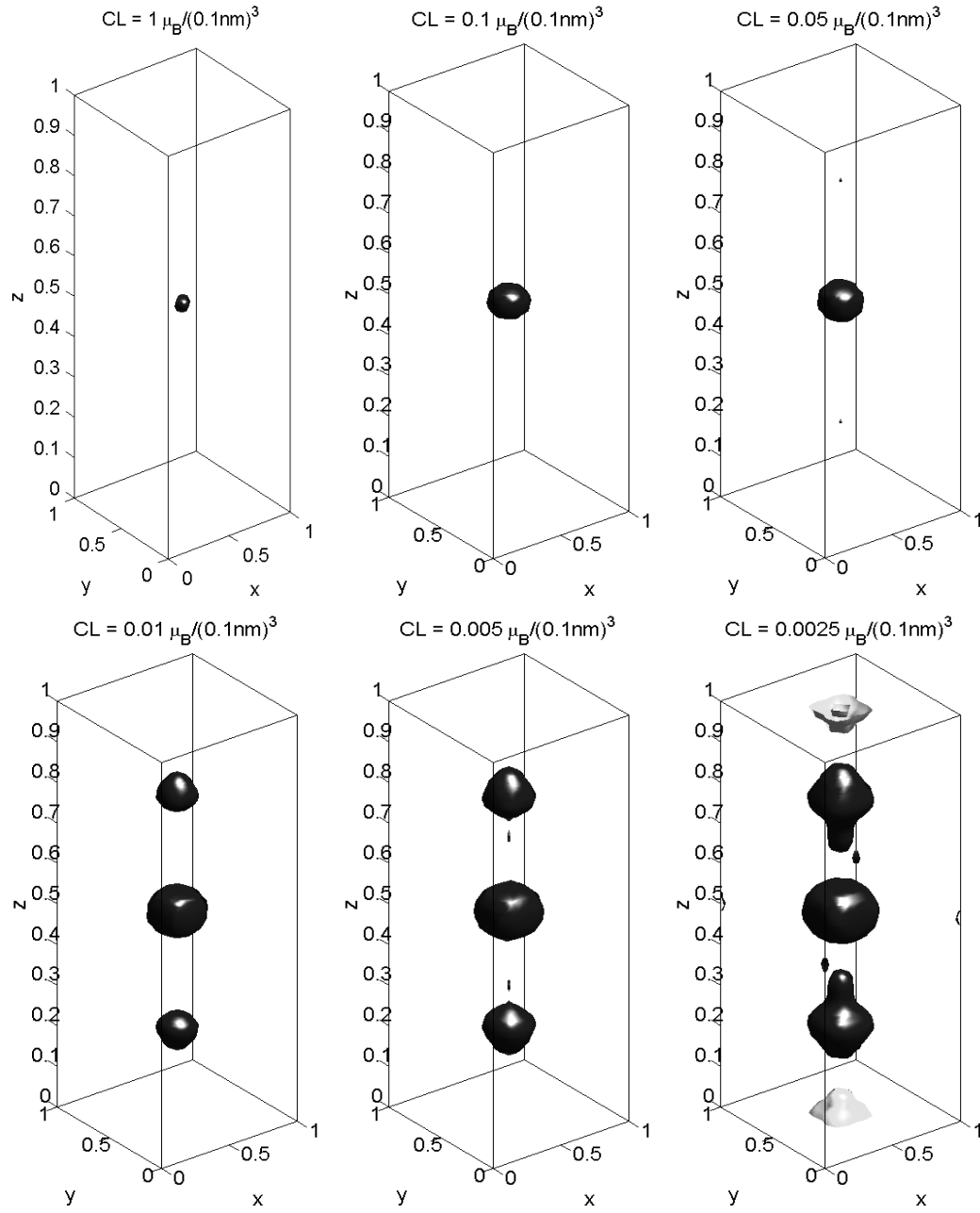


Figure 5.7: Reconstruction of the ‘averaged’ $\text{PrBa}_2\text{Cu}_3\text{O}_{6.24}$ data in tables 5.5-5.6.

$\bar{M}^s = 0.1\mu_B$ and $Q = 105$. Continues on next page.

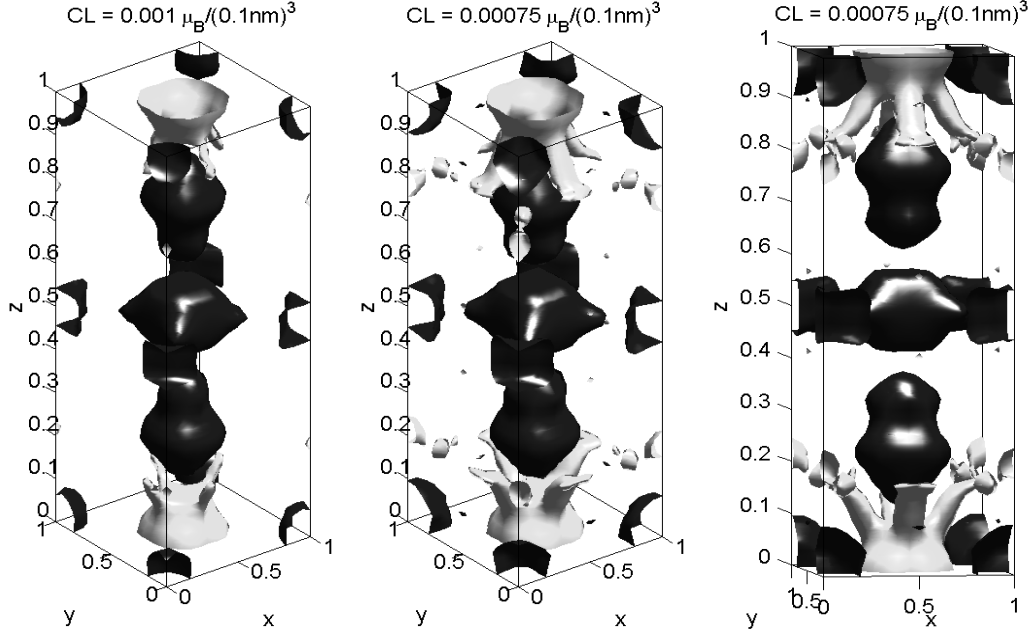


Figure 5.8: Continued from Fig. 5.7.

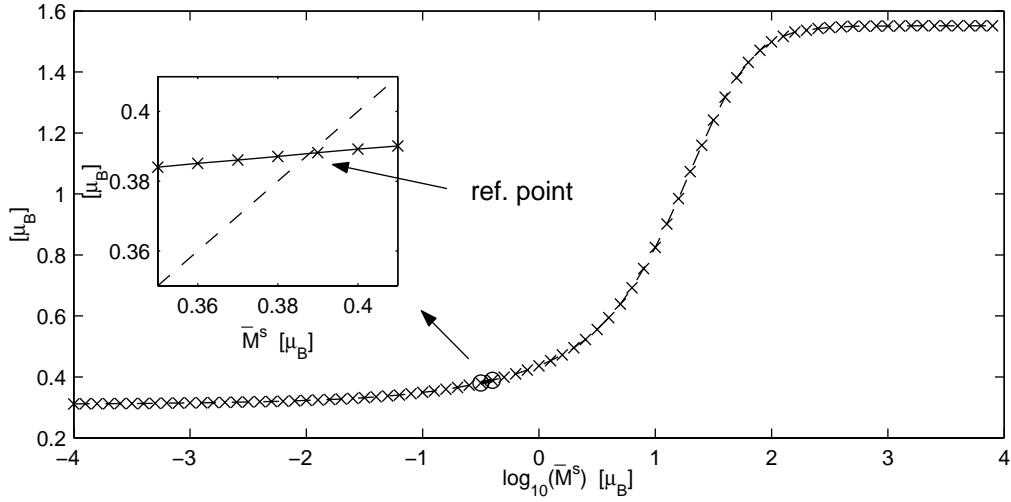


Figure 5.9: Shows the figure of merit $v \sum_i |m_i^{max}|$ as a function of \bar{M}^s for the data in tables 5.5-5.6 ($Q = 105$). The inset represents a zoom-in on the region near the reference point \bar{M}_{ref}^s estimated to $\bar{M}_{ref}^s \simeq 3.8\mu_B$. Using the recipe in Sec. 4.7, Chap. 4 this suggests that the prior constant \bar{M}^s should be selected close to $\bar{M}^s = 0.1\mu_B$.

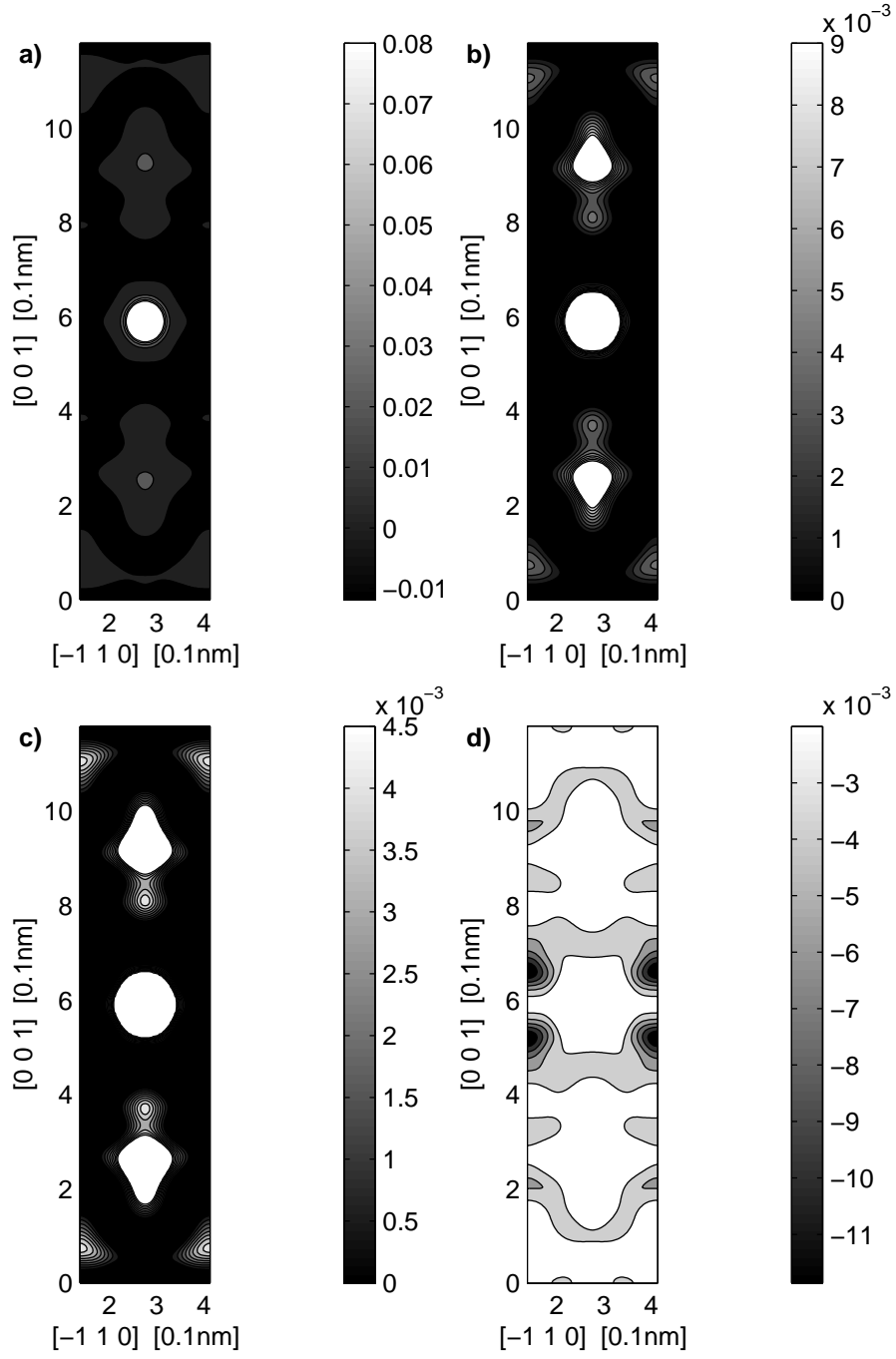


Figure 5.10: Same as in Fig. 5.4 but for the 30 structure factor data sub-set described in the text. $\bar{M}^s = 0.1\mu_B$ ($Q = P = 30$).

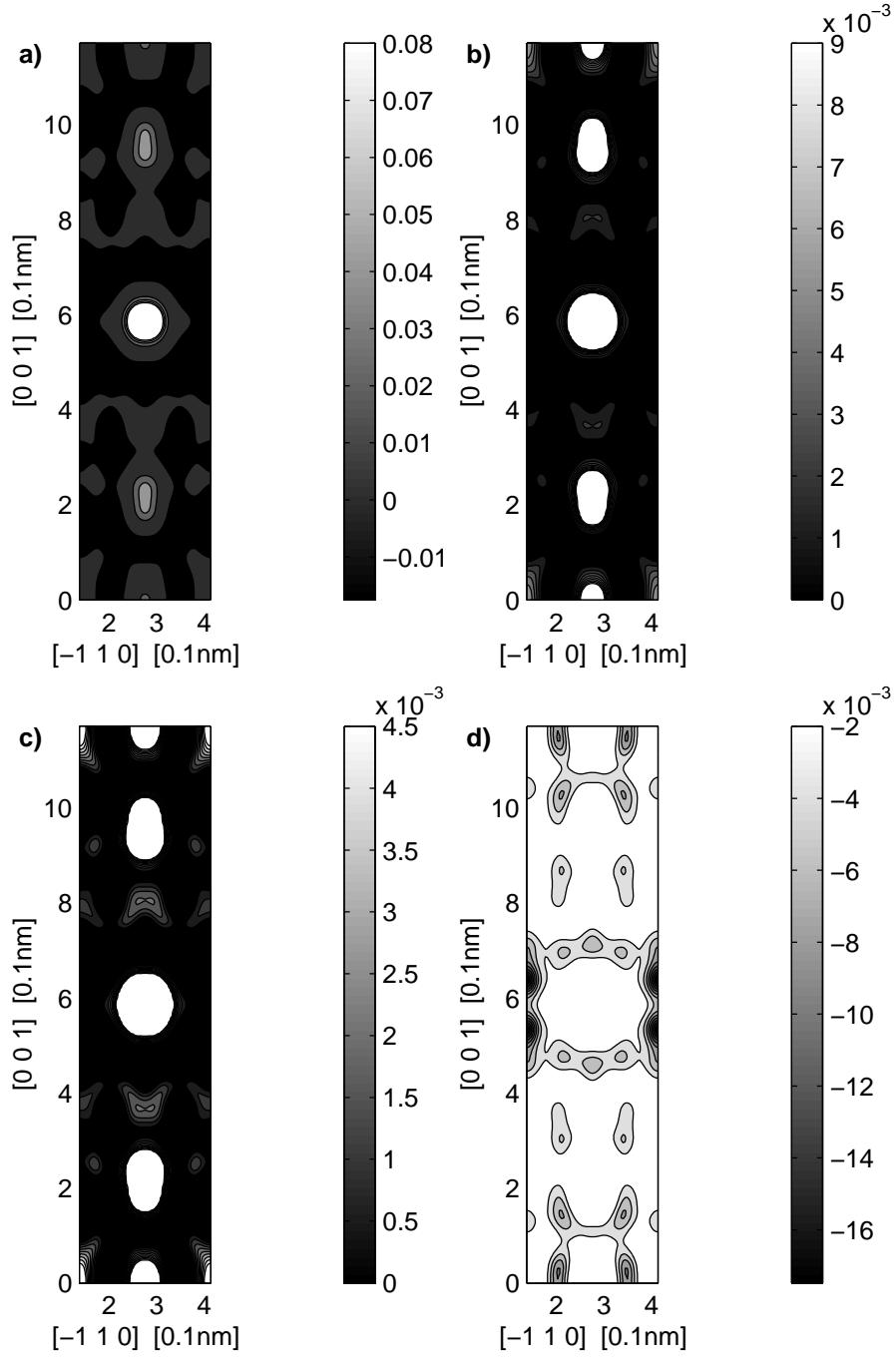


Figure 5.11: Same as in Fig. 5.4 but for the data given in table 5.7. $\bar{M}^s = 0.1\mu_B$ ($Q = P = 30$).

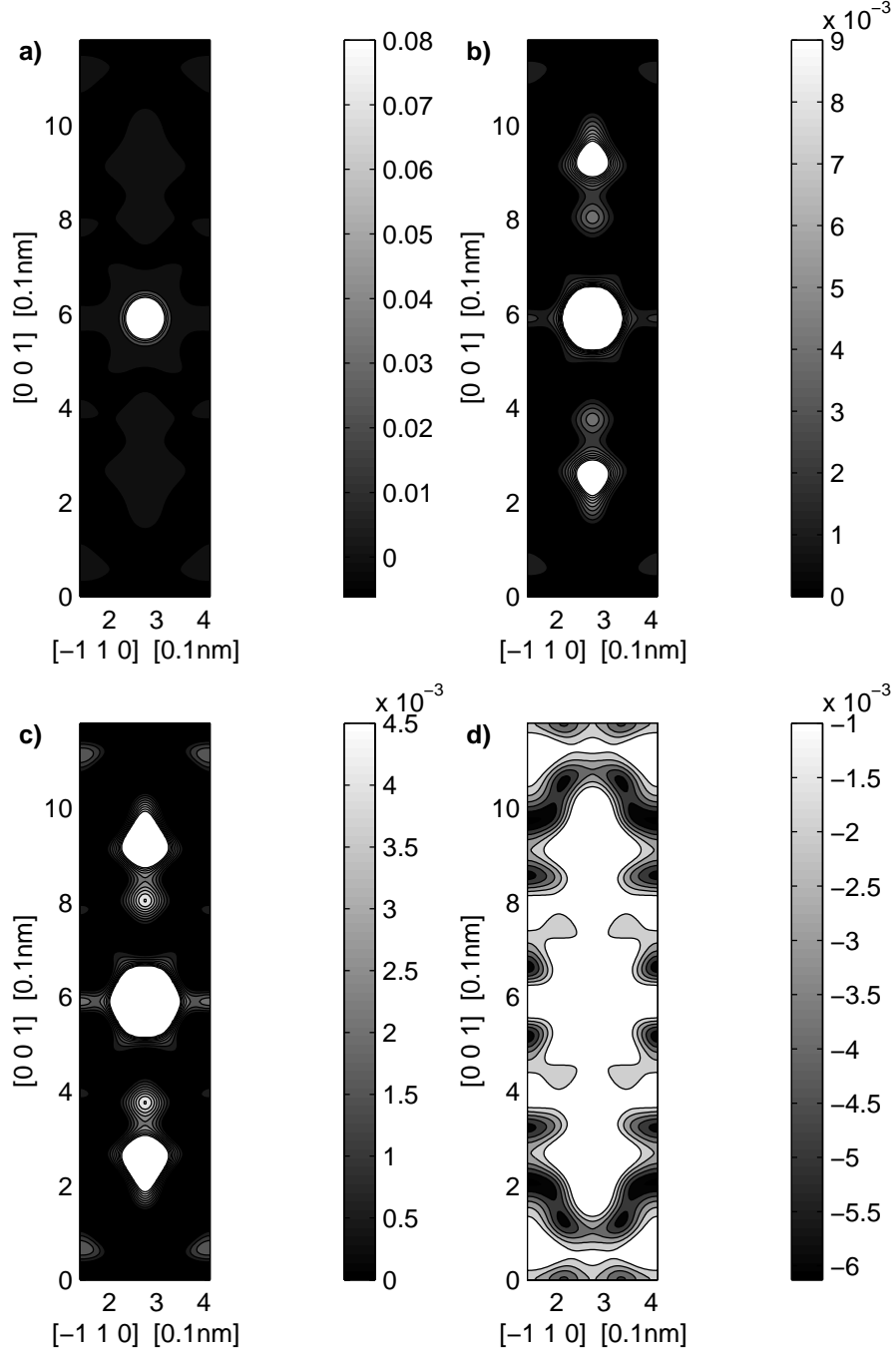


Figure 5.12: Same as in Fig. 5.10 but where the 0 0 1 and 0 0 2 structure factor in the $\mathbf{B} \parallel [1\ 1\ 0]$ columns of table 5.6 have been added to the data used to obtain the reconstruction in Fig. 5.10. $\bar{M}^s = 0.1\mu_B$ ($Q = P = 32$).

Miller indices			$\mathbf{B} \parallel [1\ 1\ 0]$		Miller indices			$\mathbf{B} \parallel [1\ 0\ 0]$	
h	k	l	$F_{hkl} [\mu_B]$	$\sigma_{hkl} [\mu_B]$	h	k	l	$F_{hkl} [\mu_B]$	$\sigma_{hkl} [\mu_B]$
0	0	6	0.20277	0.00497	0	1	0	-0.26468	0.00324
0	0	14	0.08150	0.03194	0	1	1	0.25115	0.00381
-1	1	0	0.26083	0.00209	0	1	2	-0.15615	0.00665
-1	1	1	-0.23235	0.00361	0	1	3	0.24869	0.00342
-1	1	2	0.18454	0.00907	0	1	4	-0.22842	0.00574
-1	1	3	-0.23857	0.00468	0	1	5	0.16901	0.01679
-1	1	4	0.22956	0.00651	0	1	6	-0.19589	0.00642
-1	1	6	0.19071	0.00591	0	1	7	0.20587	0.00940
-1	1	7	-0.18871	0.02693	0	1	8	-0.17158	0.01657
-1	1	8	0.15241	0.01017	0	1	9	0.14497	0.01666
-1	1	12	0.09527	0.01862	0	1	10	-0.14689	0.01096
-1	1	13	-0.08031	0.04310	0	1	11	0.16102	0.02396
-1	2	0	-0.22128	0.00615	0	1	12	-0.11327	0.04215
-1	2	1	0.19502	0.00904	0	1	13	0.13327	0.06028
-1	2	2	-0.12092	0.03144	0	1	14	-0.10895	0.03671
-1	2	3	0.21010	0.00513	0	1	16	-0.05703	0.05714
-1	2	4	-0.19940	0.00991	0	2	0	0.22949	0.00281
-1	2	6	-0.17748	0.01020	0	2	1	-0.20126	0.00731
-1	2	7	0.15539	0.02223	0	2	2	0.16382	0.01579
-1	2	8	-0.12791	0.01024	0	2	3	-0.21254	0.00624
-2	2	0	0.19310	0.00613	0	2	4	0.19731	0.00596
-2	2	1	-0.16029	0.01265	0	2	5	-0.17360	0.01037
-2	2	3	-0.17447	0.00833	0	2	6	0.17202	0.01177
-2	2	4	0.15847	0.00818	0	2	7	-0.18728	0.01274
-2	2	5	-0.15544	0.00704	0	2	8	0.14866	0.01003
-2	2	6	0.15380	0.00781	0	2	11	-0.09824	0.01487
-2	2	7	-0.13972	0.00727	0	3	0	-0.17707	0.01896
-2	2	8	0.12727	0.00691	0	3	3	0.15865	0.00945
-2	2	11	-0.07750	0.03007	0	3	4	-0.15783	0.02683
-1	3	4	0.06409	0.04017	0	3	6	-0.14440	0.01756
-2	3	0	-0.16987	0.01342	0	3	7	0.02916	0.05050
-2	3	3	0.14865	0.00776	0	3	8	-0.15290	0.02333
-2	3	6	-0.12437	0.03527	0	3	9	0.09669	0.08361
-3	3	0	0.13211	0.02068	0	3	10	-0.11438	0.02763
-3	3	3	-0.11202	0.04944	0	4	0	0.13762	0.00882
-3	3	6	0.10140	0.02731	0	4	1	-0.13746	0.01996
-2	4	0	0.11051	0.01689	0	4	4	0.11550	0.02277
-2	4	3	-0.08728	0.04690	0	4	5	-0.11624	0.02787
-2	4	4	0.11038	0.06397	0	4	6	0.13621	0.01684
-3	4	0	-0.12230	0.03199	0	5	3	-0.00554	0.04764
-3	4	3	0.07594	0.02354	0	6	0	0.06006	0.03051
-4	4	0	0.06281	0.03504	0	6	6	0.07999	0.02675
-4	4	6	0.00814	0.05156	-1	4	0	-0.13049	0.03646
					-1	5	0	0.12043	0.04355
					-1	5	1	-0.02056	0.09670
					-1	4	3	0.12088	0.03028
					-1	3	6	0.15335	0.01162
					-1	5	6	0.03401	0.05516

Table 5.5: Shows the structure factors measured with $\mathbf{B} \parallel [1\ 1\ 0]$ and $\mathbf{B} \parallel [1\ 0\ 0]$ which do not have common Miller indices.

Miller indices			$\mathbf{B} \parallel [1\ 1\ 0]$		$\mathbf{B} \parallel [1\ 0\ 0]$		Average	
h	k	l	$F_{hkl} [\mu_B]$	$\sigma_{hkl} [\mu_B]$	$F_{hkl} [\mu_B]$	$\sigma_{hkl} [\mu_B]$	$\bar{F}_{hkl} [\mu_B]$	$\bar{\sigma}_{hkl} [\mu_B]$
0	0	1	-0.25995	0.00257	-0.26136	0.00390	-0.26066	0.00324
0	0	2	0.24081	0.01055	0.23386	0.00661	0.23734	0.00858
0	0	3	-0.24396	0.00604	-0.24463	0.00415	-0.24430	0.00510
0	0	4	0.25283	0.00537	0.25112	0.00612	0.25198	0.00575
0	0	5	-0.20652	0.00447	-0.21557	0.00827	-0.21105	0.00637
0	0	7	-0.21725	0.00648	-0.22942	0.00964	-0.22334	0.00806
0	0	8	0.16286	0.01319	0.16807	0.01134	0.16547	0.01227
0	0	9	-0.09085	0.05025	-0.10146	0.02917	-0.09616	0.03971
0	0	10	0.16137	0.02497	0.18291	0.04203	0.17214	0.00335
0	0	11	-0.15583	0.00879	-0.12644	0.01349	-0.14114	0.01470
-1	3	0	0.15186	0.02465	0.21622	0.01853	0.18404	0.03218
-1	3	1	-0.17214	0.02491	-0.14432	0.03295	-0.15823	0.02893
-1	3	3	-0.17616	0.02494	-0.17237	0.02146	-0.17427	0.02320

Table 5.6: Shows the structure factors measured with $\mathbf{B} \parallel [1\ 1\ 0]$ and $\mathbf{B} \parallel [1\ 0\ 0]$ which have common Miller indices, and an estimated ‘averaged’ structure factor value and standard deviation value for each hkl set.

Miller indices					Miller indices				
h	k	l	$F_{hkl} [\mu_B]$	$\sigma_{hkl} [\mu_B]$	h	k	l	$F_{hkl} [\mu_B]$	$\sigma_{hkl} [\mu_B]$
0	0	3	-0.326	0.003	-1	1	12	0.153	0.009
0	0	4	0.31	0.007	-1	1	13	-0.137	0.01
0	0	5	-0.234	0.004	-2	2	0	0.306	0.008
0	0	6	0.314	0.003	-2	2	1	-0.174	0.006
0	0	7	-0.277	0.009	-2	2	3	-0.235	0.007
0	0	8	0.203	0.008	-2	2	4	0.238	0.011
0	0	11	-0.173	0.008	-2	2	5	-0.171	0.008
0	0	14	0.153	0.012	-2	2	6	0.235	0.009
-1	1	0	0.364	0.005	-2	2	7	-0.173	0.007
-1	1	1	-0.272	0.003	-2	2	8	0.164	0.011
-1	1	2	0.264	0.007	-2	2	11	-0.146	0.011
-1	1	3	-0.335	0.006	-3	3	0	0.205	0.011
-1	1	4	0.294	0.011	-3	3	3	-0.191	0.012
-1	1	6	0.291	0.008	-3	3	6	0.144	0.011
-1	1	8	0.193	0.006	-4	4	0	0.084	0.012

Table 5.7: Shows the structure factors measured on $\text{PrBa}_2\text{Cu}_3\text{O}_7$ from Ref. [110], page 74, which have common Miller indices with any of the data in tables 5.5-5.6.

Bibliography

- [1] A. T. Boothroyd, *J. Alloy. Compd.* **303**, 489 (2000).
- [2] J. P. Burg, Maximum entropy spectrum analysis, Oklahoma City (1967), paper presented at the 37th Ann. Intern. Meeting Soc. of Explor. Geophys.; reprinted in [35].
- [3] G. L. Squires, *Introduction to the theory of thermal neutron scattering* (Cambridge University Press, Cambridge, 1978).
- [4] S. W. Lovesey, *Theory of neutron scattering from condensed matter* (Oxford University Press, Oxford, 1987).
- [5] W. G. Williams, *Polarised neutrons* (Clarendon Press, Oxford, 1988).
- [6] G. Casella and R. L. Berger, *Statistical Inference* (Wadsworth & Brooks/Cole, Pacific Grove, California, 1990).
- [7] T. M. Apostol, *Calculus*, 2 ed. (John Wiley & Sons, Singapore, 1969), Vol. 2.
- [8] C. P. Robert, *The Bayesian choice, Springer text in statistics* (Springer-Verlag, New York, 1994).
- [9] J. M. Bernardo and A. F. M. Smith, *Bayesian theory, Wiley series in probability and mathematical statistics* (John Wiley & Sons, Chichester, 1994).

- [10] J. A. Rice, *Mathematical statistics and data analysis*, 2 ed. (Duxbury Press, Belmont, California, 1995).
- [11] M. H. Degroot, *Probability and statistics*, 2 ed. (Addison-Wesley Pub, Reading, Mass, 1986).
- [12] J. O. Berger, *Statistical decision theory and Bayesian analysis*, *Springer series in statistics*, 2 ed. (Springer-Verlag, New York, 1985).
- [13] *Encyclopedia of statistical sciences*, edited by K. Samuel, N. L. Johsson, C. B. Read, and D. L. Banks (John Wiley & Sons, New York, 1982–), vol. 1-9, update vol. 1-2.
- [14] D. S. Sivia, *Data analysis : a Bayesian tutorial* (Clarendon Press, Oxford, 1996).
- [15] J. C. Johnston, Ph.D. thesis, Oxford University, Trinity term 1996.
- [16] V. A. Macaulay, Ph.D. thesis, Oxford University, Trinity term 1992.
- [17] S. M. Ross, *Introduction to probability models*, 4 ed. (Academic Press, Boston, 1989).
- [18] A. Tarantola, *Inverse problem theory* (Elsevier, Amsterdam, 1987).
- [19] A. Papoulis, *Probability, random variables, and stochastic processes*, 3 ed. (McGraw-Hill, New York, 1991).
- [20] D. J. C. Mackay, Ph.D. thesis, California institute of technology, 1992.
- [21] E. T. Jaynes, fragments available from the author: Wayman Crow Professor of Physics, Washington University, St. Louis, 63130, USA. <ftp://bayes.wustl.edu/> (unpublished).
- [22] W. T. Grandy, *Foundations of statistical mechanics*, No. 19 in *Fundamental theories of physics* (Reidel, Dordrecht, 1987).

- [23] M. Plischke and B. Bergersen, *Equilibrium statistical physics*, 2 ed. (World Scientific, Singapore, 1994).
- [24] R. Balian, *From microphysics to macrophysics* (Springer-Verlag, Berlin; London, 1991), Vol. 1.
- [25] E. T. Jaynes, Phys. Rev. **106**, 620 (1957).
- [26] C. E. Shannon, Bell System Tech. J. **27**, 623 (1948).
- [27] T. M. Cover and J. A. Thomas, *Elements of information theory, Wiley series in telecommunications* (John Wiley & Sons, New York, 1991).
- [28] E. T. Jaynes, in *Statistical physics*, edited by K. W. Ford (W. A. Benjamin, Inc., New York, 1963), Vol. 3, p. 182, reprinted in [31], p. 39.
- [29] E. T. Jaynes, IEEE Trans. Syst. Sci. Cybern **4**, 227 (1968).
- [30] S. Kullback, *Information theory and statistics, Dover books on mathematics* (Dover, Mineola, New York, 1997).
- [31] E. T. Jaynes, in *Papers on probability, statistics and statistical physics, Synthese library*, edited by R. D. Rosenkrantz (Reidel, Dordrecht, 1983).
- [32] L. Boltzmann, *Lectures on gas theory* (Dover, New York, 1995), translated by S. G. Brush.
- [33] K. Huang, *Statistical mechanics*, 2 ed. (John Wiley & Sons, New York, 1987).
- [34] C. E. Shannon, Bell System Tech. J. **27**, 379 (1948).
- [35] D. G. Childers, *Modern spectrum analysis* (IEEE Press, New York, 1978).
- [36] E. T. Jaynes, Proc. IEEE **70**, 939 (1982).
- [37] J. Skilling and S. F. Gull, SIAM-AMS Proceedings **14**, 167 (1984).

- [38] R. Gordon, R. Bender, and G. T. Herman, J. Theor. Biol. **29**, 471 (1970).
- [39] R. Gordon and G. T. Herman, Quarterly Bull. Center for Theor. Biol., SUNY at Buffalo **4(1)**, 71 (1971).
- [40] B. R. Frieden, J. Opt. Soc. Am. **62**, 511 (1972).
- [41] S. Goldman, *Information Theory* (Prentice-Hall, New York, 1955), appendix II.
- [42] B. R. Frieden, in *Picture processing and digital filtering*, Vol. 6 of *Topics in applied physics*, edited by T. S. Huang and H. C. Andrews (Springer-Verlag, Berlin, 1975), p. 177, there also exist a 2nd corrected and revised edition of this reference: Same title and authors, Springer-Verlag, Berlin, 1979.
- [43] B. R. Frieden, Science **191**, 1237 (1976).
- [44] L. R. D’Addario, Maximum a posteriori probability and maximum entropy reconstruction, Stanford (1975), presented at Image processing for 2D and 3D reconstruction from projection: Theory and practice in medicine and the physical sciences meeting.
- [45] L. R. D’Addario, Proceedings of the Society of Photo Optical Instrumentation Engineers **231**, 2 (1980).
- [46] S. J. Wernecke and L. R. D’Addario, IEEE Trans. Comput. **C-26**, 351 (1977).
- [47] D. S. Stephenson, Progress in NMR Spectroscopy **20**, 515 (1988).
- [48] R. Narayan, Ann. Rev. Astron. Astrophys. **24**, 127 (1986).
- [49] D. L. Donoho, I. M. Johnstone, J. C. Hoch, and A. S. Stern, J. R. Statist. Soc. B **54**, 41 (1992).

- [50] B. Buck and V. A. Macaulay, in *Maximum entropy and Bayesian methods*, edited by R. Smith, G. J. Erickson, and P. O. Neudorfer (Kluwer, Dordrecht, 1992), p. 241.
- [51] V. A. Macaulay and B. Buck, Nuclear Phys. A **591**, 85 (1995).
- [52] K. Maisinger, M. P. Hobson, and A. N. Lasenby, Mon. Not. R. Astron. Soc. **290**, 313 (1997).
- [53] A. W. Jones *et al.*, Mon. Not. R. Astron. Soc. **294**, 582 (1998).
- [54] G. J. Daniell and P. J. Hore, J. Magn. Reson. **84**, 515 (1989).
- [55] W. I. F. David, Nature **346**, 731 (1990).
- [56] J. C. Hoch, A. S. Stern, D. L. Donoho, and I. M. Johnstone, J. Magn. Reson. **86**, 236 (1990).
- [57] J. C. Hoch and A. S. Stern, *NMR data processing* (Wiley-Liss, Inc., New York, 1996).
- [58] N. L. Johnson, S. Kotz, and A. W. Kemp, *Univariate discrete distributions*, 2 ed. (John Wiley & Sons, New York, 1992).
- [59] A. W. Kemp, in *Encyclopedia of statistical sciences*, edited by S. Kotz, C. B. Read, and D. L. Banks (John Wiley & Sons, New York, 1997), Vol. updata vol. 1, p. 93.
- [60] M. Abramowitz and I. A. Stegun, *Handbook of mathematical functions with formulas* (jw, New York, 1972).
- [61] H. Bateman and A. Erdélyi, *Higher transcendental functions* (McGraw-Hill, New York, 1953-55), Vol. 1-3.
- [62] G. N. Watson, *A treatise on the theory of Bessel functions*, 2nd ed. (University Press, Cambridge, 1966).

- [63] D. M. Titterton, *Astron. Astrophys* **144**, 381 (1985).
- [64] D. M. Titterton, *Int. Statist. Rev.* **53**, 141 (1985).
- [65] E. D. Laue, J. Skilling, and J. Staunton, *J. Magn. Reson.* **63**, 418 (1985).
- [66] R. J. Papoular and B. Gillon, *Europhys. Lett.* **13**, 429 (1990).
- [67] M. Sakata, T. Uno, M. Takata, and C. J. Howard, *J. Appl. Cryst.* **26**, 159 (1993).
- [68] E. D. Laue, M. R. Mayger, J. Skilling, and J. Staunton, *J. Magn. Reson.* **68**, 14 (1986).
- [69] W. I. F. David, *Inst. Phys. Conf. Ser.* **107**, 93 (1990).
- [70] R. J. Papoular and B. Gillon, in *Neutron scattering data analysis*, No. 107 in *Institute of Physics conference series*, edited by M. W. Johnson (Institute of Physics, Bristol, 1990), p. 101.
- [71] P. J. Hore, *Nuclear magnetic resonance* (Oxford University Press, Inc., New York, 1995).
- [72] P. J. Hore, D. S. Grainger, S. Wimperis, and G. J. Daniell, *J. Magn. Reson.* **89**, 415 (1990).
- [73] J. A. Jones and P. J. Hore, *J. Magn. Reson.* **92**, 276 (1991).
- [74] J. X. Boucherle *et al.*, *Physica B* **192**, 25 (1993).
- [75] A. Vernière, J. X. Boucherle, P. Lejay, and B. Gillon, *Physica B* **267-8**, 41 (1999).
- [76] A. Hiess *et al.*, *J. Phys.:Condens. Matter* **12**, 829 (2000).
- [77] L. Paolasini *et al.*, *J. Phys.: Condens. Matter* **5**, 8905 (1993).

- [78] A. Muñoz *et al.*, J. Phys.: Condens. Matter **7**, 8821 (1995).
- [79] A. Hiess *et al.*, Physica B **230-232**, 687 (1997).
- [80] L. Dobrzynski, R. J. Papoular, and M. Sakata, J. Phys. Soc. Jpn. **65**, 255 (1996).
- [81] L. Dobrzynski, R. J. Papoular, and M. Sakata, J. Magn. Magn. Mater. **140-144**, 53 (1995).
- [82] A. J. Markvardsen *et al.*, J. Magn. Magn. Mat. **177**, 502 (1998).
- [83] W. H. Press, *Numerical recipes in C*, 2nd ed. (Cambridge University Press, Cambridge, 1992).
- [84] J. Skilling and R. K. Bryan, Mon. Not. R. astr. Soc. **211**, 111 (1984).
- [85] K. Kubota, M. Takata, and M. Sakata, J. Appl. Cryst. **26**, 453 (1995).
- [86] K. Burger, Powder Diffraction **13**, 117 (1998).
- [87] S. Kumazawa, M. Takata, and M. Sakata, Acta Cryst. A **51**, 47 (1995).
- [88] K.-B. Li, A. S. Stern, and J. C. Hoch, J. Magn. Reson. **134**, 161 (1998).
- [89] A. J. Freeman and R. E. Watson, Phys. Rev. **127**, 2058 (1962).
- [90] J. Skilling, in *Maximum entropy and Bayesian methods*, edited by J. Skilling (Kluwer Academic Pub., London, 1989), p. 45.
- [91] S. F. Gull, in *Maximum entropy and Bayesian methods*, edited by J. Skilling (Kluwer Academic Pub., London, 1989), p. 53.
- [92] S. F. Gull and J. Skilling, Technical report, Maximum Entropy Data Consultants Ltd, Meldreth, Royston SG8 6NR, England (unpublished).
- [93] H. B. Radousky, J. Mater. Res. **7**, 1917 (1992).

- [94] R. Fehrenbacher and T. M. Rice, Phys. Rev. Lett. **70**, 3471 (1993).
- [95] A. T. Boothroyd *et al.*, Phys. Rev. Lett. **78**, 130 (1997).
- [96] C. Wilkinson, H. W. Khamis, R. F. D. Stansfield, and G. J. McIntyre, J. Appl. Cryst. **21**, 471 (1988).
- [97] A. Renault *et al.*, J. Physique **48**, 1407 (1987).
- [98] G. J. McIntyre, A. Renault, and G. Collin, Phys. Rev. B **37**, 5148 (1988).
- [99] A. T. Boothroyd, S. M. Doyle, and R. Osborn, Physica C **217**, 425 (1993).
- [100] E. Balcar, J. Phys. C **8**, 1975 (1975).
- [101] E. U. Condon and H. Odabaşı, *Atomic structure* (Cambridge University Press, New York, 1980).
- [102] C. Stassis and H. W. Deckman, Phys. Rev. B **13**, 4934 (1976).
- [103] G. B. Folland, *Fourier analysis and its applications* (Brooks/Cole Pub. Com., Pacific Grove, 1992).
- [104] J. X. Boucherle *et al.*, Physica C **162-4**, 1285 (1989).
- [105] J. Y. Henry *et al.*, Physica C **235-240**, 1659 (1994).
- [106] B. Gillon, Physica B **174**, 340 (1991).
- [107] B. Gillon *et al.*, Physica C **162-4**, 1275 (1989).
- [108] B. Gillon *et al.*, Physica B **156-7**, 851 (1989).
- [109] M. P. Nutley, A. T. Boothroyd, and G. J. McIntyre, J. Magn. Magn. Mat. **104-7**, 623 (1992).
- [110] M. P. Nutley, Ph.D. thesis, Warwick University, March 1994.

- [111] G. L. Goodman, C. K. Loong, and L. Soderholm, J. Phys.: Condens. Matter **3**, 49 (1991).
- [112] H.-D. Jostarndt *et al.*, Phys. Rev. B **46**, 14872 (1992).
- [113] G. Hilscler *et al.*, Phys. Rev. B **49**, 535 (1994).
- [114] S. J. S. Lister *et al.*, Physica C **317-8**, 572 (1999).
- [115] Z. Zou *et al.*, Phys. Rev. Lett. **80**, 1074 (1998).
- [116] J. Ye *et al.*, Phys. Rev. B **58**, R619 (1998).
- [117] H. A. Mook, Phys. Rev. **148**, 495 (1966).
- [118] F. Maniawski, B. v. Laar, and S. Kaprzyk, J. Phys. F.: Metal Phys. **11**, 1895 (1981).
- [119] M. Sakata and M. Sato, Acta. Cryst. A **46**, 263 (1992).
- [120] M. Sakata, T. Uno, M. Takata, and R. Mori, Acta. Cryst. B **48**, 591 (1992).
- [121] S. Kumazawa, Y. Kubota, M. Takata, and M. Sakata, J. Appl. Cryst. **26**, 453 (1993).
- [122] R. J. Papoular, E. Ressouche, J. Schweizer, and A. Zheludev, in *Maximum entropy and Bayesian methods*, edited by A. Mohammad-Djafari and G. Demoments (Kluwer, Dordrecht, 1993), p. 311.
- [123] R. J. Papoular and A. Delapalme, Phys. Rev. Lett. **72**, 1486 (1994).
- [124] R. J. Papoular, Y. Vekhter, and P. Coppers, Acta. Cryst. **A52**, 397 (1996).
- [125] R. J. Papoular, W. Prandl, and J. Schweizer, in *Maximum entropy and Bayesian methods*, edited by C. R. Smith, G. J. Erickson, and P. O. Neudorfer (Kluwer, Dordrecht, 1992), p. 359.

- [126] D. M. Collins, *Nature* **298**, 49 (1982).
- [127] R. W. H. Sargent, in *Numerical methods for constrained optimization*, edited by P. E. Gill, W. Murray, and R. Fletcher (Academic Press, London, 1974), p. 149.